Since January 2020 Elsevier has created a COVID-19 resource centre with free information in English and Mandarin on the novel coronavirus COVID-19. The COVID-19 resource centre is hosted on Elsevier Connect, the company's public news and information website.

Cell

Virological characteristics of the SARS-CoV-2 Omicron BA.2 spike

Graphical abstract

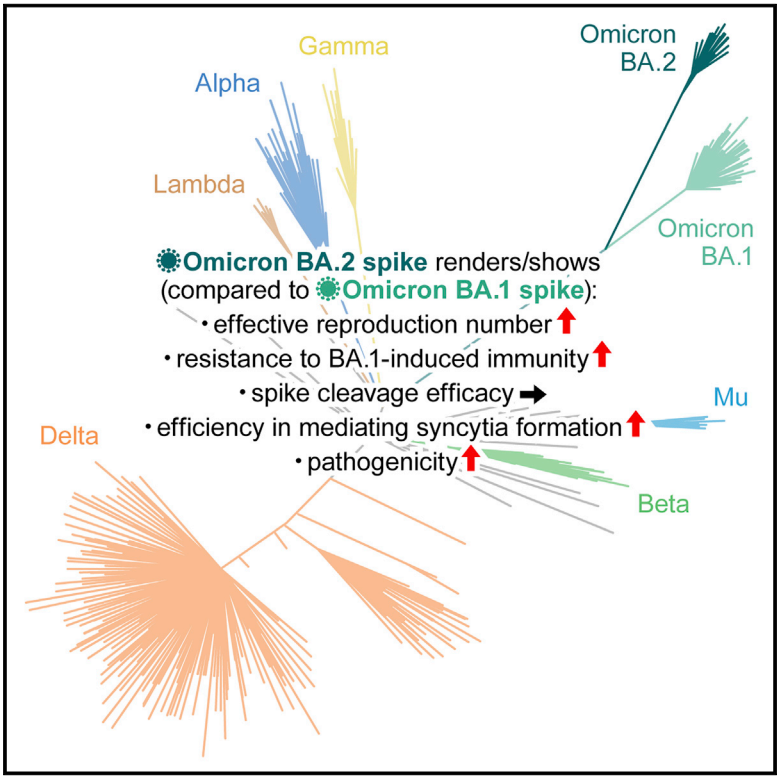

Highlights

- The effective reproduction number of BA.2 is 1.4-fold higher than that of BA.1
- BA.2 is resistant to BA.1-induced humoral immunity
- The BA.2 spike is more fusogenic than BA.1 spike
- BA.2 spike-bearing virus is more pathogenic than BA.1 spike-bearing virus

Authors

Daichi Yamasoba, Izumi Kimura, Hesham Nasser, ..., Takasuke Fukuhara, Terumasa Ikeda, Kei Sato

Correspondence

sakatsuki@cc.miyazaki-u.ac.jp (A.S.), tirie@hiroshima-u.ac.jp (T.I.), tanaka@med.hokudai.ac.jp (S.T.), matsuk@czc.hokudai.ac.jp (K.M.), fukut@pop.med.hokudai.ac.jp (T.F.), ikedat@kumamoto-u.ac.jp (T.I.), keisato@g.ecc.u-tokyo.ac.jp (K.S.)

In brief

Yamasoba and G2P-Japan Consortium et al. elucidate the characteristics of SARS-CoV-2 Omicron variant BA.2—transmissibility, immune resistance, virological property, and pathogenicity. The effective population number of BA.2 is higher than that of BA.1, and the antigenicity of BA.2 is different from that of BA.1. The BA.2 spike is more fusogenic than the BA.1 spike, and notably, the BA.2 spike-bearing virus is more pathogenic than the BA.1 spike-bearing virus. This multiscale investigation suggests the potential risk of BA.2 to global health.

Yamasoba et al., 2022, Cell *185*, 2103–2115
June 9, 2022
https://doi.org/10.1016/j.cell.2022.04.035

CellPress

Cell

CellPress
OPEN ACCESS

Article

Virological characteristics of the SARS-CoV-2 Omicron BA.2 spike

Daichi Yamasoba,[1,2,33] Izumi Kimura,[1,33] Hesham Nasser,[3,4,33] Yuhei Morioka,[5,33] Naganori Nao,[6,7,33] Jumpei Ito,[1,33] Keiya Uriu,[1,8,33] Masumi Tsuda,[9,10,33] Jiri Zahradnik,[11,33] Kotaro Shirakawa,[12] Rigel Suzuki,[5] Mai Kishimoto,[13] Yusuke Kosugi,[1,14,15] Kouji Kobiyama,[16,17] Teppei Hara,[16] Mako Toyoda,[18] Yuri L. Tanaka,[19] Erika P. Butlertanaka,[19] Ryo Shimizu,[3] Hayato Ito,[5] Lei Wang,[9,10] Yoshitaka Oda,[9] Yasuko Orba,[13,19] Michihito Sasaki,[13,20] Kayoko Nagata,[12] Kumiko Yoshimatsu,[21] Hiroyuki Asakura,[22] Mami Nagashima,[22] Kenji Sadamasu,[22] Kazuhisa Yoshimura,[22] Jin Kuramochi,[23] Motoaki Seki,[24] Ryoji Fujiki,[24] Atsushi Kaneda,[24] Tadanaga Shimada,[25] Taka-aki Nakada,[25]

(Author list continued on next page)

[1]Division of Systems Virology, Department of Microbiology and Immunology, The Institute of Medical Science, The University of Tokyo, Tokyo, Japan
[2]Faculty of Medicine, Kobe University, Kobe, Japan
[3]Division of Molecular Virology and Genetics, Joint Research Center for Human Retrovirus infection, Kumamoto University, Kumamoto, Japan
[4]Department of Clinical Pathology, Faculty of Medicine, Suez Canal University, Ismailia, Egypt
[5]Department of Microbiology and Immunology, Graduate School of Medicine, Hokkaido University, Sapporo, Japan
[6]Division of International Research Promotion, International Institute for Zoonosis Control, Hokkaido University, Sapporo, Japan
[7]One Health Research Center, Hokkaido University, Sapporo, Japan
[8]Graduate School of Medicine, The University of Tokyo, Tokyo, Japan
[9]Department of Cancer Pathology, Faculty of Medicine, Hokkaido University, Sapporo, Japan
[10]Institute for Chemical Reaction Design and Discovery (WPI-ICReDD), Hokkaido University, Sapporo, Japan
[11]Department of Biomolecular Sciences, Weizmann Institute of Science, Rehovot, Israel
[12]Department of Hematology and Oncology, Graduate School of Medicine, Kyoto University, Kyoto, Japan
[13]Division of Molecular Pathobiology, International Institute for Zoonosis Control, Hokkaido University, Sapporo, Japan
[14]Laboratory of Systems Virology, Institute for Frontier Life and Medical Sciences, Kyoto University, Kyoto, Japan
[15]Graduate School of Pharmaceutical Sciences, Kyoto University, Kyoto, Japan
[16]Division of Vaccine Science, Department of Microbiology and Immunology, The Institute of Medical Science, The University of Tokyo, Tokyo, Japan
[17]International Vaccine Design Center, The Institute of Medical Science, The University of Tokyo, Tokyo, Japan
[18]Division of Infection and immunity, Joint Research Center for Human Retrovirus infection, Kumamoto University, Kumamoto, Japan
[19]Department of Veterinary Science, Faculty of Agriculture, University of Miyazaki, Miyazaki, Japan
[20]International Collaboration Unit, International Institute for Zoonosis Control, Hokkaido University, Sapporo, Japan

(Affiliations continued on next page)

SUMMARY

Soon after the emergence and global spread of the SARS-CoV-2 Omicron lineage BA.1, another Omicron lineage, BA.2, began outcompeting BA.1. The results of statistical analysis showed that the effective reproduction number of BA.2 is 1.4-fold higher than that of BA.1. Neutralization experiments revealed that immunity induced by COVID vaccines widely administered to human populations is not effective against BA.2, similar to BA.1, and that the antigenicity of BA.2 is notably different from that of BA.1. Cell culture experiments showed that the BA.2 spike confers higher replication efficacy in human nasal epithelial cells and is more efficient in mediating syncytia formation than the BA.1 spike. Furthermore, infection experiments using hamsters indicated that the BA.2 spike-bearing virus is more pathogenic than the BA.1 spike-bearing virus. Altogether, the results of our multiscale investigations suggest that the risk of BA.2 to global health is potentially higher than that of BA.1.

INTRODUCTION

The virological characteristics of newly emerging SARS-CoV-2 variants, such as their transmissibility, pathogenicity, and resistance to vaccine-induced immunity and antiviral drugs, represent an urgent global health concern. In March 2022, the Omicron variant (B.1.1.529 and BA lineages) is the most recently recognized variant of concern, and it has spread worldwide

Seiichiro Sakao,[26] Takuji Suzuki,[26] Takamasa Ueno,[18] Akifumi Takaori-Kondo,[12] Ken J. Ishii,[16,17] Gideon Schreiber,[11] The Genotype to Phenotype Japan (G2P-Japan) Consortium, Hirofumi Sawa,[6,7,13,20] Akatsuki Saito,[19,27,28,*] Takashi Irie,[29,*] Shinya Tanaka,[9,10,*] Keita Matsuno,[7,20,30,*] Takasuke Fukuhara,[5,*] Terumasa Ikeda,[3,*] and Kei Sato[1,8,17,31,32,34,35,*]

[21]Institute for Genetic Medicine, Hokkaido University, Sapporo, Japan
[22]Tokyo Metropolitan Institute of Public Health, Tokyo, Japan
[23]Interpark Kuramochi Clinic, Utsunomiya, Japan
[24]Department of Molecular Oncology, Graduate School of Medicine, Chiba University, Chiba, Japan
[25]Department of Emergency and Critical Care Medicine, Graduate School of Medicine, Chiba University, Chiba, Japan
[26]Department of Respirology, Graduate School of Medicine, Chiba University, Chiba, Japan
[27]Center for Animal Disease Control, University of Miyazaki, Chiba, Japan
[28]Graduate School of Medicine and Veterinary Medicine, University of Miyazaki, Miyazaki, Japan
[29]Institute of Biomedical and Health Sciences, Hiroshima University, Hiroshima, Japan
[30]Division of Risk Analysis and Management, International Institute for Zoonosis Control, Hokkaido University, Sapporo, Japan
[31]International Research Center for Infectious Diseases, The Institute of Medical Science, The University of Tokyo, Tokyo, Japan
[32]CREST, Japan Science and Technology Agency, Kawaguchi, Japan
[33]These authors contributed equally
[34]Twitter: @SystemsVirology
[35]Lead contact
*Correspondence: sakatsuki@cc.miyazaki-u.ac.jp (A.S.), tirie@hiroshima-u.ac.jp (T.I.), tanaka@med.hokudai.ac.jp (S.T.), matsuk@czc.hokudai.ac.jp (K.M.), fukut@pop.med.hokudai.ac.jp (T.F.), ikedat@kumamoto-u.ac.jp (T.I.), keisato@g.ecc.u-tokyo.ac.jp (K.S.)
https://doi.org/10.1016/j.cell.2022.04.035

(WHO, 2022). Omicron was first reported in South Africa at the end of November 2021 (WHO, 2021). Soon after its emergence, a variant of Omicron, the BA.1 lineage, rapidly spread worldwide and outcompeted other variants, such as Delta. Since then, another variant of Omicron, the BA.2 lineage, was detected (March 2022) in multiple countries, such as Denmark and the UK (UKHSA, 2022). Notably, BA.2 has begun outcompeting BA.1 (UKHSA, 2022), suggesting that BA.2 is more transmissible than BA.1.

The virological characteristics of SARS-CoV-2 variants, such as the antigenicity and infection route into the cells, are determined by the spike (S) protein. The precursor of the SARS-CoV-2 S protein is initially cleaved in infected cells by a cellular protease, furin, yielding two subunits, S1 and S2 (reviewed in V'Kovski et al., 2021). The S1 subunit binds to human angiotensin converting enzyme 2 (ACE2), and SARS-CoV-2 utilizes this molecule as the receptor for cell entry (Hoffmann et al., 2020). After binding to ACE2, SARS-CoV-2 invades the cells via transmembrane serine protease 2 (TMPRSS2)-dependent or -independent pathways. In the former pathway, the S2 subunit is processed by another cellular protease, TMPRSS2, which is expressed on the cell surface, and the viral particle then fuses with the plasma membrane. In the latter pathway, the viral particle bound to ACE2 is endocytosed independently of TMPRSS2, and then the S2 subunit on the viral particle is processed by the cellular proteases expressed in endosomes (e.g., cathepsin), leading to viral fusion [reviewed in (V'Kovski et al., 2021)]. Since the BA.2 S protein bears >30 mutations compared with the original SARS-CoV-2 strain (B lineage, strain Wuhan-Hu-1, GenBank: NC_045512.2) (Wu et al., 2020), it is feasible to assume that the virological features of BA.2 are dramatically different from those of the original virus as well as the other variants.

A few months after the emergence of BA.1, we and others revealed the virological characteristics of this variant (Cameroni et al., 2022; Cao et al., 2021; Cele et al., 2021; Dejnirattisai et al., 2021, 2022; Garcia-Beltran et al., 2021; Halfmann et al., 2022; Han et al., 2022; Liu et al., 2021a; Meng et al., 2022; Planas et al., 2021; Shuai et al., 2022; Suzuki et al., 2022; Takashita et al., 2022; VanBlargan et al., 2022). For instance, BA.1 is highly resistant to vaccine-induced humoral immunity (Cameroni et al., 2022; Cao et al., 2021; Cele et al., 2021; Dejnirattisai et al., 2021, 2022; Garcia-Beltran et al., 2021; Liu et al., 2021a; Meng et al., 2022; Planas et al., 2021; Takashita et al., 2022; VanBlargan et al., 2022). Additionally, the S protein of BA.1 is less efficiently cleaved by furin and less fusogenic than those of the Delta variant and an ancestral SARS-CoV-2 variant belonging to the B.1.1 lineage (Meng et al., 2022; Suzuki et al., 2022), and the pathogenicity of BA.1 is attenuated relative to that of Delta and the ancestral B.1.1 virus (Halfmann et al., 2022; Shuai et al., 2022; Suzuki et al., 2022). However, the virological characteristics of BA.2 remain poorly understood.

RESULTS

Phylogenetic and epidemic dynamics of BA.2

Omicron has been classified into three main lineages: BA.1, BA.2, and BA.3. As a sublineage of BA.1, BA1.1 harbors an R346K substitution in its S protein (Figure 1A). Although these lineages are monophyletic, their sequences have greatly diversified. For example, BA.1 differs from BA.2 by 50 amino acids, which is approximately twice the number found among four other variants of concern (Alpha, Beta, Gamma, and Delta) and Wuhan-Hu-1, a prototypical SARS-CoV-2 isolate (Figure 1B). Phylodynamic analysis has suggested that BA.1 emerged first, followed by BA.2 and BA.3 (Figure S1). In addition to BA.1, the earlier strains of BA.2, BA.3, and BA.1.1 were isolated in Gauteng Province, South Africa, the site of the earliest Omicron (BA.1) epidemic (Figure S1) (Viana et al., 2022). These results suggest that the remarkable diversification of Omicron probably occurred around Gauteng Province and that all Omicron lineages emerged there.

Although BA.1 spread worldwide earlier than BA.2, since January 2022, the lineage frequency of BA.2 has increased and exceeded that of BA.1 in multiple countries, such as the

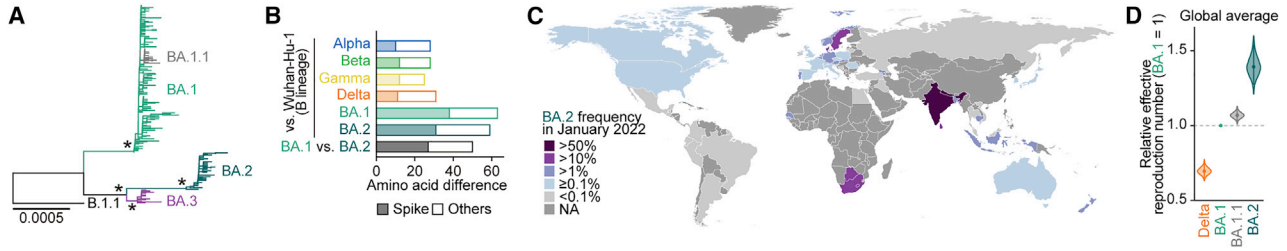

Figure 1. BA.2 epidemic

(A) Maximum likelihood tree of the Omicron lineages sampled from South Africa. The asterisks indicate the nodes with ≥0.95 bootstrap values.

(B) Number of amino acid differences detected between the different viral lineages in the S region (filled) and other regions (opened).

(C) Relative frequency of BA.2 according to genome surveillance data in January 2022. The values of countries with ≥20 available SARS-CoV-2 sequences are shown.

(D) Estimated relative effective reproduction number of each viral lineage, assuming a fixed generation time of 2.1 days. The global average value estimated by a Bayesian hierarchical model is shown. The value of each country is shown in Figure S2D. The posterior distribution (violin), 95% CI (line), and posterior mean (dot) are shown.

See also Figures S1 and S2; Table S1.

Philippines, India, Denmark, Singapore, Austria, and South Africa (Figures 1C and S2). To quantify the growth advantage of BA.2 in the population, we constructed a Bayesian hierarchical model representing the epidemic dynamics of SARS-CoV-2 lineages. This hierarchical model can estimate the global average value of the relative effective reproduction number of each viral lineage (Figure 1D) as well as the number in each country (Figure S2). The effective reproduction number of BA.2 is 1.40-fold higher than that of BA.1 on average worldwide [95% confidence interval (CI), 1.27–1.56; Figure 1D]. Furthermore, the effective reproduction number of BA.2 is even higher than that of BA.1.1 (Figures 1D and S2D). These results suggest that the BA.2 epidemic will further expand around the world, highlighting the importance of elucidating the virological features of BA.2 in depth.

Immune resistance of BA.2

Since the sequence of BA.2 (particularly that of the S protein) is substantially different from that of BA.1 (Figures 1B and 2A), it is reasonable to assume that the virological properties of BA.2, such as its immune resistance and pathogenicity, are also different. To elucidate the virological features of BA.2, we set out to perform a neutralization assay using pseudoviruses and the neutralizing antibodies elicited by vaccination. Consistent with recent studies (Cameroni et al., 2022; Cao et al., 2021; Cele et al., 2021; Dejnirattisai et al., 2021, 2022; Garcia-Beltran et al., 2021; Liu et al., 2021a; Meng et al., 2022; Planas et al., 2021; Takashita et al., 2022; VanBlargan et al., 2022), BA.1 was found to be highly resistant to the antisera elicited by the mRNA-1273, ChAdOx1, and BNT162b2 vaccines (Figures 2B–2D). Similar to BA.1, BA.2 was also highly resistant to vaccine-induced antisera (Figures 2B–2D). On the other hand, the sera obtained 1 month after the 3rd dose of the BNT162b2 vaccine showed that both of BA.1 and BA.2 could be neutralized, but the neutralization levels were still lower than those of B.1.1 and Delta (Figure 2D). Additionally, BA.2 was almost completely resistant to two therapeutic monoclonal antibodies, casirivimab and imdevimab, and was 35-fold more resistant to another therapeutic antibody, sotrovimab, than the ancestral D614G-bearing B.1.1 virus (Figure 2E). Moreover, both BA.1 and BA.2 were highly resistant to convalescent sera from individuals who had been infected with an early pandemic virus (collected before May 2020) and the Alpha and Delta variants (Figure 2F). These data suggest that similar to BA.1, BA.2 is highly resistant to antisera induced by vaccination or infection with other SARS-CoV-2 variants as well as three antiviral therapeutic antibodies.

We next tested the 21 sera infected with BA.1 from 13 convalescents who were fully vaccinated (2 shots), 1 convalescent who was 1-dose vaccinated, and 7 convalescents who were not vaccinated (Table S2). BA.1 convalescent sera exhibited the strongest antiviral effect against BA.1 (Figure 2F). Regarding the case of the BA.1-infected sera with full vaccination, the antiviral effects against BA.1 and BA.2 were comparable (Figure 2F). On the other hand, it is interesting to note that compared with the BA.1 variant, the BA.2 variant was significantly (4.1-fold) more resistant to the BA.1-infected sera from convalescents without full vaccination (Figure 2F; $p = 0.016$ by the Wilcoxon signed-rank test), suggesting that the BA.1 infection without vaccination cannot elicit efficient antiviral humoral immunity against BA.2. Importantly, the sera from fully vaccinated BA.1-infected convalescents exhibited significantly stronger antiviral effects against all variants tested than those from unvaccinated or 1-dose vaccinated convalescents (Figure 2G), suggesting that BA.1 infection without vaccination cannot elicit efficient antiviral humoral immunity.

To further address the possibility that BA.1-induced humoral immunity is less effective against BA.2, we used convalescent sera obtained from infected hamsters at 16 days postinfection (d.p.i.). Similar to the results of experiments involving convalescent human sera (Figure 2F), both BA.1 and BA.2 exhibited pronounced resistance against B.1.1- and Delta-infected convalescent hamster sera (Figure 2H). More importantly, BA.2 was significantly (2.9-fold) more resistant to BA.1-infected convalescent hamster sera than BA.1 (Figure 2H; $p = 0.031$ by the Wilcoxon signed-rank test), which is consistent with the observation using human sera (Figure 2F). Moreover, mice were immunized with cells expressing the S proteins of ancestral B.1.1, BA.1, and BA.2 viruses, and murine antisera were

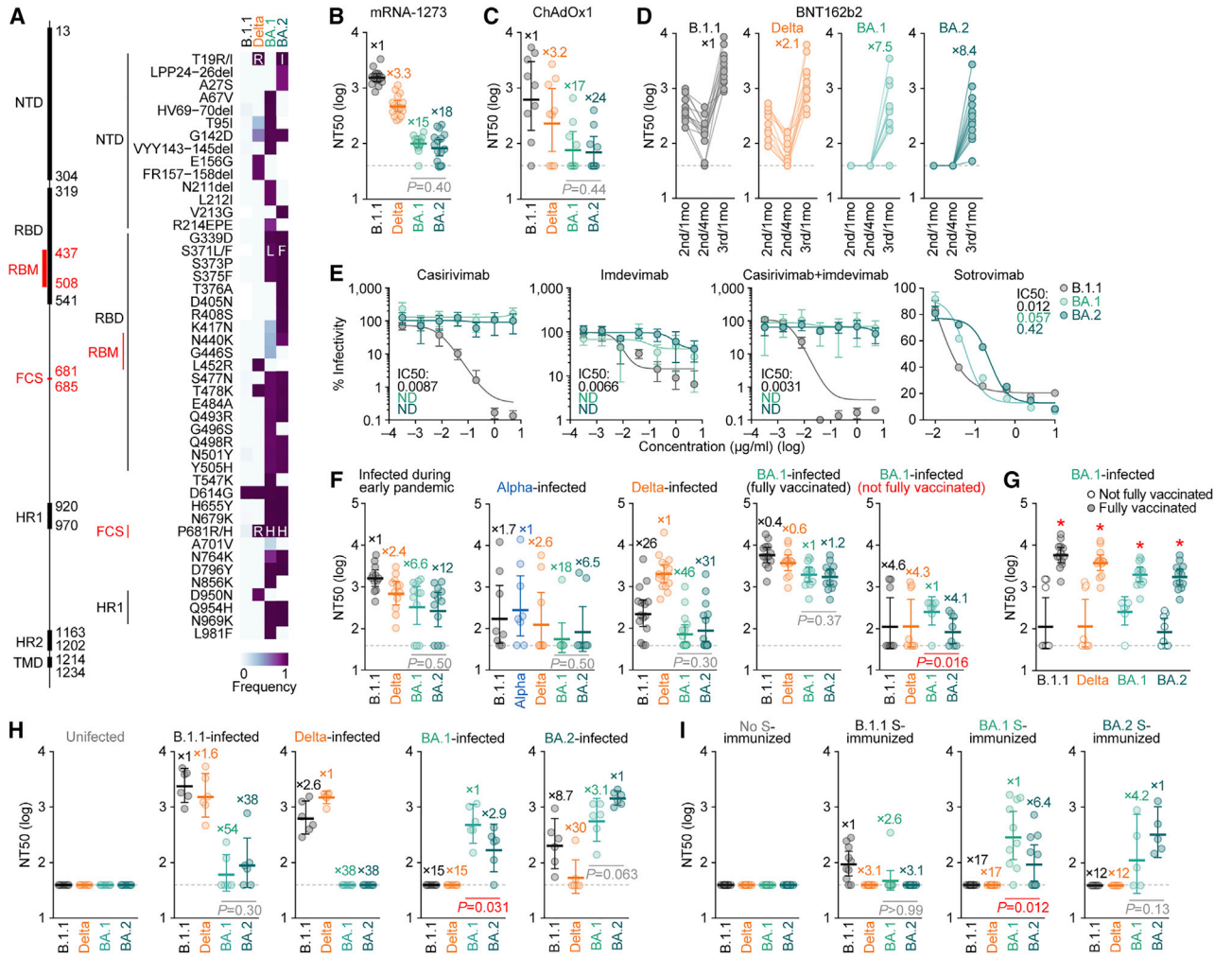

Figure 2. Immune resistance of BA.2

(A) Amino acid substitutions in S. Left, primary structure and domains of the virus. The numbers indicate the amino acid positions. NTD, N-terminal domain; RBM, receptor-binding motif; HR, heptad repeat; TMD, transmembrane domain. Right, heatmap showing the frequency of amino acid substitutions. Substitutions detected in >10% of sequences of any lineage are shown.

(B–I) Neutralization assays. Neutralization assays were performed with pseudoviruses harboring the S proteins of B.1.1 (the D614G-bearing ancestral virus), Delta, BA.1 and BA.2, and the following sera and monoclonal antibodies.

(B) mRNA-1273 vaccine (16 donors).

(C) ChAdOx1 vaccine (9 donors).

(D) BNT162b2 vaccine (13 donors). 2nd/1mo, 1 month after the 2nd dose; 2nd/4mo, 4 months after the 2nd dose; 3rd/1mo, 1 month after the 3rd dose.

(E) Therapeutic monoclonal antibodies (casirivimab, imdevimab, casirivimab + imdevimab, and sotrovimab). IC50, 50% inhibitory concentration; ND, not determined.

(F and G) Convalescent sera from individuals infected with an early pandemic virus (until May 2020) (12 donors), Alpha (8 donors), Delta (15 donors), or BA.1 [13 fully vaccinated donors or 8 not fully vaccinated donors].

(H) Sera from uninfected, B.1.1-infected, Delta-infected, BA.1-infected, and BA.2-infected hamsters at 16 d.p.i. (6 hamsters per each group).

(I) Sera from mice immunized with empty vector-transfected cells (10 mice), cells expressing B.1.1 S (10 mice) or BA.1 S (H, right; 10 mice) were used.

In (B)–(D) and (F)–(I), assays with each serum sample were performed in triplicate to determine the 50% neutralization titer (NT50). Each dot represents one NT50 value, and the geometric mean and 95% CI are shown. The numbers indicate the fold changes of resistance versus each antigenic variant. The horizontal dashed line indicates the detection limit (40-fold). Statistically significant differences between BA.1 and BA.2 were determined by two-sided Wilcoxon signed-rank tests (B, C, F, H, and I) or two-sided Mann-Whitney U tests (G, * $p < 0.05$). Information on the vaccinated/convalescent donors is summarized in Table S2.

In (E), the assays for each concentration were performed in triplicate, and the presented data are expressed as the average ± SD.

See also Table S2.

collected. Again, the neutralization assay using murine sera showed that compared with BA.1, BA.2 is more significantly (6.4-fold) resistant to BA.1 S-immunized sera (Figure 2I; $p = 0.012$ by the Wilcoxon signed-rank test). Again, these findings suggest that BA.1-induced humoral immunity is less effective against BA.2. In contrast to the resistance of BA.2 to

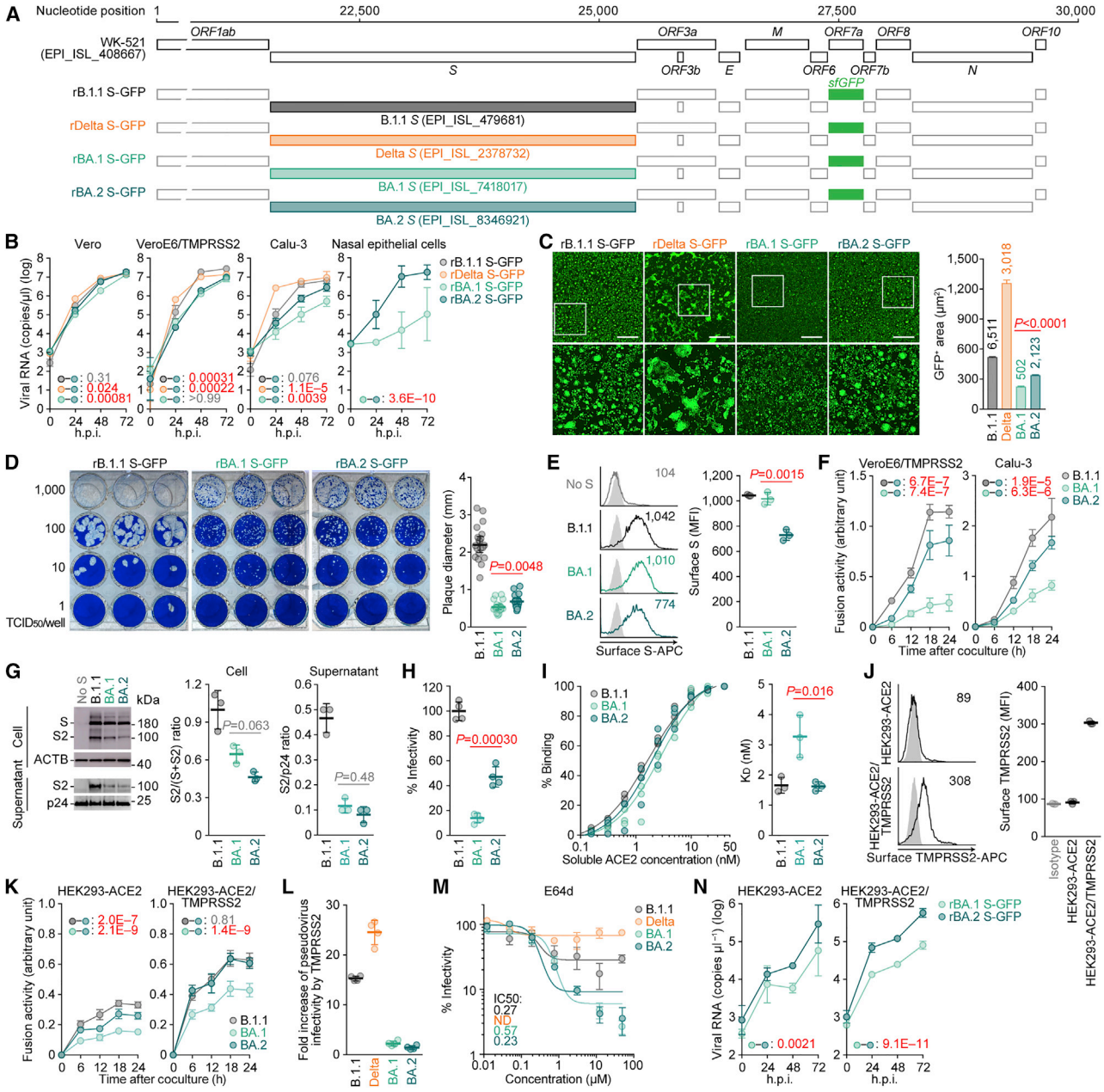

Figure 3. Virological features of BA.2 *in vitro*

(A) Scheme for the chimeric recombinant SARS-CoV-2 used in this study. The SARS-CoV-2 genome and its genes are shown. The template was SARS-CoV-2 strain WK-521 (PANGO lineage A, GISAID ID: EPI_ISL_408667), and the *S* genes were swapped with those of the respective lineages/strains (GISAID IDs are indicated in the figure). *ORF7a* was swapped with the *sfGFP* gene.

(B) Growth kinetics of chimeric recombinant SARS-CoV-2 in Vero cells, VeroE6/TMPRSS2 cells, Calu-3 cells, and human nasal epithelial cells.

(C) Fluorescence microscopy. The GFP area was measured in infected VeroE6/TMPRSS2 cells (multiplicity of infection [m.o.i.] 0.01) at 48 h.p.i. Left, representative panels. Higher-magnification views of the regions indicated by squares are shown at the bottom. Representative time-course data are shown in Figure S2E. Scale bars, 500 μm. Right, the summarized results. The numbers in the panel indicate the numbers of GFP-positive cells counted.

(D) Plaque assay. Representative panels (left) and a summary of the recorded plaque diameters (20 plaques per virus) (right) are shown.

(E) S expression on the cell surface. Representative histograms stained with an anti-S1/S2 polyclonal antibody (left) and the summarized data (right) are shown. In the left panel, the number in the histogram indicates mean fluorescence intensity (MFI). Gray histograms indicate isotype controls.

(F) S-based fusion assay. The recorded fusion activity (arbitrary units) is shown.

(G) Western blotting. Left, representative blots of S-expressing cells (top) and pseudovirus (bottom). ACTB is an internal control for the cells, whereas HIV-1 p24 is an internal control for the pseudovirus. kDa, kilodalton. Middle, the ratio of S2 to the full-length S plus S2 proteins in the cells. Right, the ratio of S2 to HIV-1 p24 in the pseudovirus (supernatant).

(legend continued on next page)

BA.1-induced humoral immunity (Figures 2F, 2H, and 2I), the sensitivity of BA.1 to BA.2-induced humoral immunity in rodents was comparable with that of BA.2 (Figures 2H and 2I). These data suggest that BA.2-induced immunity is cross-reactive with BA.1.

Virological features of BA.2 *in vitro*

To investigate the virological characteristics of BA.2, we generated chimeric recombinant SARS-CoV-2 that expresses GFP and harbors the *S* gene of ancestral B.1.1, Delta, BA.1, or BA.2 by reverse genetics (rB.1.1 S-GFP, rDelta S-GFP, rBA.1 S-GFP, and rBA.2-GFP, respectively, summarized in Figure 3A) (Torii et al., 2021). Although the growth of rBA.1 S-GFP and rBA.2 S-GFP in VeroE6/TMPRSS2 cells was comparable, rBA.2 S-GFP was more replicative than rBA.1 S-GFP in Calu-3 cells and primary human nasal epithelial cells (Figure 3B). Notably, the morphology of the infected cells differed; rBA.2 S-GFP formed significantly (1.52-fold) larger syncytia than rBA.1 S-GFP (Figures 3C and S3A). However, the plaque size of VeroE6/TMPRSS2 cells infected with rBA.1 S-GFP and rBA.2 S-GFP was significantly smaller than that of VeroE6/TMPRSS2 cells infected with rB.1.1 S-GFP, and the plaques that formed following rBA.2 S-GFP infection were significantly (1.27-fold) larger than those that formed following rBA.1 S-GFP infection (Figure 3D). Moreover, coculture of S-expressing cells with HEK293-ACE2/TMPRSS2 cells showed that BA.2 S induced the formation of significantly (2.9-fold) larger multinuclear syncytia than BA.1 S (Figure S3B). These data suggest that BA.2 is more fusogenic than BA.1. To further explore this possibility, we analyzed the efficiency in mediating syncytia formation of BA.2 S (Motozono et al., 2021; Saito et al., 2022; Suzuki et al., 2022). The expression level of BA.2 S on the cell surface was significantly lower than that of BA.1 S (Figure 3E). Nevertheless, our fusion assays using VeroE6/TMPRSS2 cells and Calu-3 cells showed that BA.2 S is significantly more efficient in mediating syncytia formation than BA.1 S (Figure 3F).

Because we have proposed that SARS-CoV-2 S-mediated fusogenicity is closely associated with the efficiency of S1/S2 cleavage (Saito et al., 2022; Suzuki et al., 2022), we hypothesized that BA.2 S is more efficiently cleaved than BA.1 S. However, western blotting analysis showed that BA.2 S is less efficiently cleaved than B.1.1 S and that the cleavage efficiencies of BA.1 S and BA.2 S are comparable (Figure 3G). These data suggest that BA.2 S exhibits a higher fusogenicity independent of S1/S2 cleavage.

Next, we assessed the features of pseudoviruses. The levels of cleaved S2 in viruses pseudotyped with BA.1 S and BA.2 S were comparable, whereas these S2 levels were lower than those pseudotyped with B.1.1 S (Figure 3G). However, the pseudovirus infectivity of BA.2 S was significantly higher than that of BA.1 S (Figure 3H). We then analyzed the binding affinity of the BA.2 S receptor-binding domain (RBD) toward ACE2 in a yeast surface display assay (Dejnirattisai et al., 2022; Kimura et al., 2022; Motozono et al., 2021). Although the binding affinity of BA.1 S RBD toward ACE2 is controversial (Cameroni et al., 2022; Dejnirattisai et al., 2022; Han et al., 2022; Meng et al., 2022; Schubert et al., 2022; Wu et al., 2022), our yeast surface display assay showed that the binding affinity of the BA.2 S RBD is significantly higher than that of the BA.1 S RBD (Figure 3I).

We have recently revealed that BA.1 poorly utilizes TMPRSS2 for infection (Meng et al., 2022). To analyze TMPRSS2 utilization by BA.2 S, we performed a cell-based fusion assay using 293-ACE2 cells with or without TMPRSS2 expression. We verified that endogenous TMPRSS2 was undetectable on the surface of 293-ACE2 cells (Figure 3J). As shown in Figure 3K, the efficiency in mediating syncytia formation of BA.2 S was significantly higher than that of BA.1 in both cell lines. However, although BA.2 S was less fusogenic than B.1.1 S in 293-ACE2 cells, the efficiency in mediating syncytia formation of BA.2 S and B.1.1 S in 293-ACE2/TMPRSS2 cells was comparable (Figure 3K). These results suggest that the relatively higher fusogenicity of BA.2 is dependent on TMPRSS2 expression on the surface of the target cell. To further assess whether a TMPRSS2-dependent increase in infection was also observed when cell-free virus was used, we inoculated 293-ACE2 cells and 293-ACE2/TMPRSS2 cells with pseudoviruses. Although the infectivity of B.1.1 and Delta was increased 15.3-fold and 24.6-fold, respectively, when TMPRSS2 was expressed on the target cell, the level of TMPRSS2 expression did not affect the infectivity of either BA.1 or BA.2 (Figure 3L). These results suggest that TMPRSS2 does not affect the infectivity of cell-free BA.2 virus.

Our recent study showed that BA.1 prefers the endocytic entry pathway rather than the TMPRSS2-mediated cell surface entry pathway (Meng et al., 2022). To address whether BA.2 also

(H) Pseudovirus assay. The percent infectivity compared with that of the virus pseudotyped with B.1.1 S are shown.
(I) Binding affinity of SARS-CoV-2 S RBD to ACE2 by yeast surface display. The percentage of SARS-CoV-2 S RBD expressed on yeast binding to soluble ACE2 (left) and the summarized K_D values (right) are shown.
(J) TMPRSS2 expression on the cell surface. Representative histograms stained with an anti-TMPRSS2 polyclonal antibody (left) and the summarized data (right) are shown. In the left panel, the number in the histogram indicates MFI. Gray histograms indicate the isotype controls.
(K) S-based fusion assay. The recorded fusion activity (arbitrary units) is shown.
(L) Fold increase in pseudovirus infectivity based on TMPRSS2 expression.
(M) E64d treatment. IC50, 50% inhibitory concentration; ND, not determined.
(N) Growth kinetics of chimeric recombinant SARS-CoV-2 in HK293-ACE2 and HEK293-ACE2/TMPRSS2 cells.
Assays were performed in quadruplicate (B, H, L, J, and N), octuplicate (B, most right) or triplicate (E–G, I, J, K, and M), and the presented data are expressed as the average ± SD. Each dot indicates the result of an individual plaque (D) and an individual replicate (E, G– J, L and I).
Statistically significant differences between BA.2 and other variants across time points were determined by multiple regression (B, F, K, and N). Family-wise error rates (FWERs) calculated using the Holm method are indicated in the figures. Statistically significant differences between BA.1 and BA.2 were determined by two-sided Mann-Whitney U tests (C and D), two-sided Student's t tests (E, H, and I), or two-sided paired t test (G).
See also Figure S3.

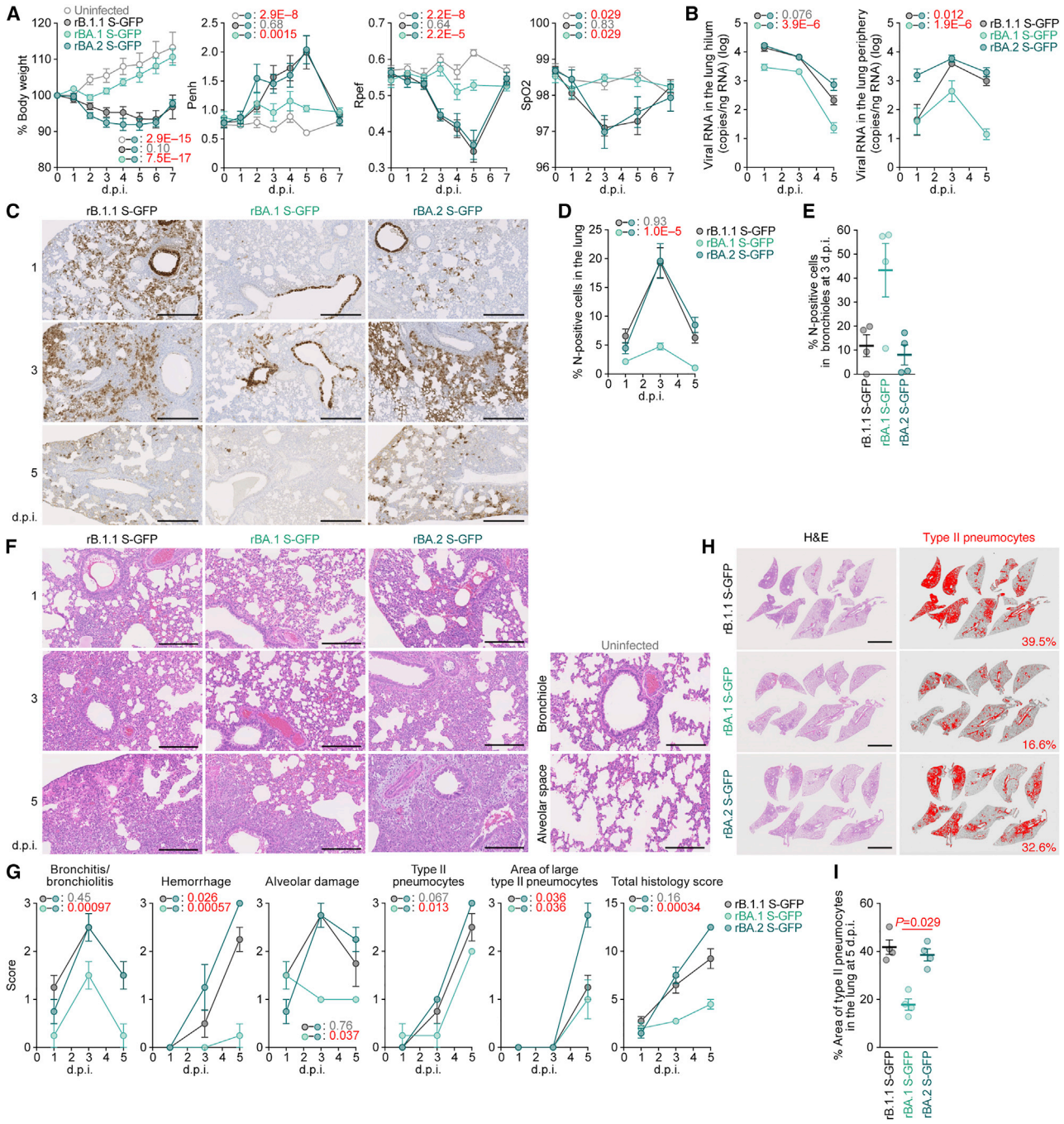

Figure 4. Virological features of BA.2 *in vivo*

Syrian hamsters were intranasally inoculated with rB.1.1 S-GFP, rBA.1 S-GFP, and rBA.2 S-GFP.

(A) Body weight, Penh, Rpef, and SpO_2 values were routinely measured. Hamsters of the same age were intranasally inoculated with PBS (uninfected).

(B) Viral RNA loads in the lung hilum (left) and periphery (right).

(C) IHC of the viral N protein in the lungs at 1, 3, and 5 d.p.i of all infected hamsters (n = 4 per viral strain). Scale bars, 500 μm.

(D and E) Percentage of N-positive cells in whole lung lobes (D) and bronchioles in the frontal/upper lung lobe at 3 d.p.i. (E) measured by IHC. In (D), the raw data are shown in Figure S4B.

(F) H&E staining of the lungs of infected hamsters. Uninfected lung alveolar space and bronchioles are also shown.

(G) Histopathological scoring of lung lesions. Representative pathological features are reported in our previous studies (Saito et al., 2022; Suzuki et al., 2022).

(H and I) Type II pneumocytes in the lungs of infected hamsters. (H) Lung lobes of infected hamsters at 5 d.p.i. In each panel, H&E staining (left) and the digitalized inflammation area (right, indicated in red) are shown. The number in the right panel indicates the percentage of the section represented by the indicated area (i.e., the area indicated in red within the total area of the lung lobe). (I) The summarized data.

(legend continued on next page)

prefers the endocytic entry route, E64d, a cathepsin inhibitor that blocks the endocytosis-dependent entry of SARS-CoV-2 (Zhao et al., 2021), was used. Consistent with a previous report (Meng et al., 2022), Delta was resistant to E64d (Figure 3M). In contrast, both BA.1 and BA.2 were sensitive to E64d (Figure 3M). We verified that the inhibitory activity of E64d with concentrations did not show cytotoxicity in our experimental setup (Figure S3C). These data suggest that the BA.2 virus prefers the endocytosis-dependent entry pathway.

Finally, we investigated the growth of BA.2 in the presence or absence of TMPRSS2. Although the growth of rBA.1 S-GFP and rBA.2 S-GFP was comparable in 293-ACE2 cells, rBA.2 S-GFP was more replicative than rBA.1 S-GFP in 293-ACE2/TMPRSS2 cells (Figure 3N). Overall, our data suggest that the BA.2 S is involved in stronger efficiency in mediating syncytia formation and more efficient replication than the BA.1 S in a TMPRSS2-dependent manner.

Virological features of BA.2 *in vivo*

To investigate the dynamics of the viral replication of SARS-CoV-2 carrying the BA.2 S *in vivo*, we conducted hamster infection experiments using the chimeric recombinant SARS-CoV-2 described above (Figure 3A). Consistent with our recent study using clinical B.1.1 and BA.1 isolates (Suzuki et al., 2022), rB.1.1 S-GFP-infected hamsters exhibited decreased body weight and respiratory disorders, as reflected by two surrogate markers of bronchoconstriction or airway obstruction (enhanced pause [Penh] and the ratio of time to peak expiratory follow relative to the total expiratory time [Rpef]), as well as decreased subcutaneous oxygen saturation (SpO_2). However, the rBA.1 S-GFP-infected hamsters exhibited no respiratory disorder or only slight effects (Figure 4A). Notably, all of the routinely measured parameters, including body weight, Penh, Rpef, and SpO_2, were significantly different between rBA.2 S-GFP-infected hamsters and uninfected or rBA.1 S-GFP-infected hamsters but were comparable between rBA.2 S-GFP-infected and rB.1.1 S-GFP-infected hamsters (Figure 4A). These data suggest that the BA.2 S confers higher pathogenicity compared with the BA.1 S.

To analyze viral spread in the respiratory organs of infected hamsters, the viral RNA load and nucleocapsid (N) expression were assessed by RT-qPCR analysis of viral RNA and immunohistochemistry (IHC), respectively. As shown in Figure 4B, the viral RNA loads in the two lung regions (hilum and periphery) of rBA.2 S-GFP-infected hamsters were significantly higher than those of rBA.1 S-GFP-infected hamsters. In the lung periphery, the viral RNA load of rBA.2 S-GFP was significantly higher than that of rB.1.1 S-GFP, and the viral RNA load of rBA.2 S-GFP at 1 d.p.i. was 11-fold and 9.3-fold higher than those of rB.1.1 S-GFP and rBA.1 S-GFP, respectively, at the same time point (Figure 4B). To address the possibility that the BA.2 S-carrying SARS-CoV-2 spreads more efficiently than the BA.1 S-carrying virus, we investigated N protein positivity in the trachea and the lung area close to the hilum. At 1 d.p.i., N protein was detectable in the lower tracheal epithelium in all infected hamsters, and its expression was particularly salient in the middle portion of the trachea in rBA.2 S-GFP-infected hamsters (Figure S4A). N protein positivity was observed in both the bronchial and bronchiolar epithelia in all infected lungs (Figure 4C). Notably, alveolar positivity was observed in rB.1.1 S-GFP- and rBA.2 S-GFP-infected lungs but not in rBA.1 S-GFP-infected lungs (Figure 4C). Morphometry showed that the percentage of N-positive cells in rBA.2 S-GFP-infected lungs was significantly higher than that in rBA.1 S-GFP-infected lungs and peaked at 3 d.p.i. (Figures 4D and S4B). On the other hand, the percentage of N-positive cells in the bronchus/bronchioles of rBA.2 S-GFP-infected hamsters at 3 d.p.i. was 5.4-fold lower than that in rBA.1 S-GFP-infected hamsters (Figure 4E). At 5 d.p.i., N protein expression had almost disappeared in rBA.1 S-GFP-infected lungs, whereas alveolar staining was still detectable in rB.1.1 S-GFP- and rBA.2 S-GFP-infected lungs (Figures 4C, 4D, and S4B). These data suggest that the BA.2 S contributes to more efficient viral spread though lung tissues compared with the BA.1 S.

Pathogenicity of BA.2

To investigate the pathogenicity of BA.2, the right lungs of infected hamsters were collected at 1, 3, and 5 d.p.i. and subjected to hematoxylin and eosin (H&E) staining and histopathological analysis (Saito et al., 2022; Suzuki et al., 2022). All histopathological parameters of rBA.2 S-GFP-infected hamsters, including bronchitis/bronchiolitis, hemorrhage, alveolar damage, and the levels of type II pneumocytes, were significantly higher than those of rBA.1 S-GFP-infected hamsters (Figures 4F and 4G). The hemorrhage score, including congestive edema, was significantly higher for rBA.2 S-GFP than for rB.1.1 S-GFP (Figure 4G). As shown in our previous studies (Saito et al., 2022; Suzuki et al., 2022), hyperplastic large type II pneumocytes, indicating the severity of inflammation, were observed in all the infected hamsters at 5 d.p.i., and the area of large type II pneumocytes in rBA.2 S-GFP-infected hamsters was significantly larger than that in in rB.1.1 S-GFP- and rBA.1 S-GFP-infected hamsters (Figure 4G). The total histology score of rBA.2 S-GFP was significantly higher than that of rBA.1 S-GFP (Figure 4G). Furthermore, in rBA.2 S-GFP- and rB.1.1 S-GFP-infected lungs, inflammation with type II alveolar pneumocyte hyperplasia was found in each lobe, especially in the frontal/upper and accessary lobes (Figures 4H, 4I, and S4C).

DISCUSSION

Although BA.2 is considered an Omicron variant, its genomic sequence is much different from that of BA.1, which suggests

Data are presented as the average (A, 6 hamsters per group; B–I, 4 hamsters per group) ± SEM. In (E) and (I), each dot indicates the result of an individual hamster. In (A), (B), (D), and (G), statistically significant differences between BA.2 and other variants or uninfected hamsters across time points were determined by multiple regression. The 0 d.p.i. data were excluded from the analyses. The FWERs calculated using the Holm method are indicated in the figures.
In (I), the statistically significant differences between rBA.1 S-GFP and rBA.2 S-GFP were determined by a two-sided Mann-Whitney U test.
In (C), (F), and (H), each panel shows a representative result from an individual infected hamster. Scale bars, 500 μm (C); 250 μm (F); or 5 mm (H).
See also Figure S4.

that the virological characteristics of BA.2 are different from those of BA.1. Herein, we elucidated the virological characteristics of BA.2, which included a higher effective reproduction number and higher fusogenicity and higher pathogenic potential than BA.1. We demonstrated that BA.2 is resistant to BA.1-induced humoral immunity. Using a hamster model and chimeric recombinant viruses harboring the *S* genes of SARS-CoV-2 variants, we showed that the BA.2 S-bearing virus is more pathogenic than the BA.1 S-bearing virus. Together, our data indicate that BA.2 is virologically distinct from BA.1.

Using three different types of antisera obtained from BA.1-infected individuals and experimental animals (BA.1-infected hamsters and the mice immunized with BA.1 S protein), we demonstrated the resistance of BA.2 to BA.1-induced humoral immunity. Our results indicate that the antigenicity of BA.2 is different from that of BA.1. Additionally, we demonstrated that sera from individuals with breakthrough BA.1 infection (i.e., BA.1 infection after the 2nd vaccination dose) exhibited robust antiviral immunity against BA.1, BA.2, and the other variants tested. On the other hand, sera from BA.1-infected individuals without full vaccination (i.e., only the 1st dose or no vaccination) showed poor antiviral activity against all SARS-CoV-2 variants tested. These data suggest that the antiviral effects of BA.1 infection alone cannot match those of a live attenuated vaccine, but BA.1 infection after full vaccination can boost antiviral effects.

The higher fusogenicity of BA.2 S was a pronounced characteristic observed in the in vitro experiments. The results indicated that Delta S is more highly fusogenic than BA.1 S and B.1.1 S; hence, we hypothesized that the higher fusogenicity could be attributed to the higher efficiency of S cleavage (Meng et al., 2022; Mlcochova et al., 2021; Saito et al., 2022; Suzuki et al., 2022). However, BA.2 S exhibited higher fusogenicity than BA.1 S without an increase in S cleavage efficiency. In recent studies (Saito et al., 2022; Suzuki et al., 2022), we proposed that the fusogenicity of the SARS-CoV-2 variant is closely related to its pathogenicity. This hypothesis was further supported by the results for the BA.2 S-bearing virus in the present study. However, unlike Delta, the higher fusogenicity of BA.2 does not appear to be attributed to a higher efficiency of S cleavage (Meng et al., 2022; Mlcochova et al., 2021; Saito et al., 2022; Suzuki et al., 2022). Moreover, although TMPRSS2 increased the efficiency of both cell-cell fusion (Saito et al., 2022) and cell-free infection mediated by B.1.1 S and Delta S, TMPRSS2 increased the efficiency of BA.2 S-mediated cell-cell fusion but did not affect the efficiency of BA.2 S-mediated cell-free infection. These observations suggest that TMPRSS2 contributes to cell-cell fusion and cell-free infection mediated by BA.2 S via different mechanisms of action.

In our prior studies, which focused on the Delta (Saito et al., 2022) and Omicron/BA.1 (Meng et al., 2022; Suzuki et al., 2022) variants, SARS-CoV-2 S-mediated fusogenicity was closely associated with the efficiency of S1/S2 cleavage. However, although BA.2 S exhibited higher fusogenicity than BA.1 S, the cleavage efficiency of BA.2 S was comparable with that of the BA.1 S. Additionally, BA.2 S-mediated cell-cell fusion was enhanced by TMPRSS2 expression, whereas BA.2 S-mediated cell-free infection was not, as it favors the TMPRSS2-independent endocytosis-dependent pathway. Although the difference in TMPRSS2 preference between the cell-cell and cell-free BA.2 infection pathways is of scientific interest, the mechanism of action remains unclear. By fully elucidating this mechanism, the virological features of BA.2 could be understood, including its possibly higher pathogenicity, as observed in the hamsters infected with rBA.2 S-GFP virus.

The most critical finding affecting global health is that the BA.2 S-bearing virus exhibits higher pathogenicity than the BA.1 S-bearing virus. Although the BA.2 pathogenicity should be evaluated by clinical studies in depth, our investigations using a hamster model and chimeric recombinant viruses showed that the pathogenicity of the BA.2 S-bearing virus is similar to that of the B.1.1 S-bearing virus and higher than that of the BA.1 S-bearing virus. More importantly, the viral RNA load at the lung periphery and the histopathological disorders associated with BA.2 were more severe than those associated with BA.1 and even B.1.1. Together with the higher effective reproduction number and pronounced immune resistance of BA.2, it is evident that the spread of BA.2 may be a serious global health issue in the near future. In summary, our data suggest that BA.2 may be the most concerning variant for global health identified thus far.

Limitations of the study

Here, we showed that a recombinant BA.2 virus (rBA.2 S-GFP) is more pathogenic than a recombinant BA.1 virus (rBA.1 S-GFP) in an experimental hamster model (Figure 4). In contrast, it has been recently reported that the risks of infection by and hospitalization from BA.2 are comparable with those of BA.1 in the human population (Qassim et al., 2022; Wolter et al., 2022). This discrepancy might be due to differences between experimental animal models and humans, and findings about disease severity in the hamster model may not reflect the course of human disease with BA.2. However, it should be noted that in recent studies (Qassim et al., 2022; Wolter et al., 2022), most of individuals surveyed have been vaccinated or experienced previous SARS-CoV-2 infections. Because experimental hamsters are immunologically naive, the differences in the results observed between experimental animals and humans might be due to this difference in immunological status. In fact, as of April 2022, a large surge of BA.2 infection, with relatively higher severity and increased hospitalization rates, has been reported from Hong Kong, where the vaccination rate in elderly people is not very high (HKSAR, 2022). This might be due to the potentially greater pathogenicity of BA.2.

Another limitation of the present study is the use of a chimeric recombinant SARS-CoV-2, rBA.2 S-GFP virus, which harbors the BA.2 *S* gene in a non-BA.2 (PANGO lineage A) genomic backbone (Figure 3A), instead of a genuine BA.2 virus. Therefore, the virological features of rBA.2 S-GFP may not completely reflect those of BA.2. For example, although we showed that rBA.2 S-GFP is more pathogenic than rBA.1 S-GFP in a hamster model, a recent study using a clinical isolate of BA.2 showed that the pathogenicity of BA.2 is similar to that of BA.1 in animal models (Kawaoka et al., 2022). The inconsistency of BA.2 pathogenicity found between our study and other's (Kawaoka et al., 2022) can be explained by the

possibility that the BA.2 S is potentially pathogenic, but the non-*S* region of the BA.2 genome could attenuate its viral pathogenicity. Moreover, we should emphasize the possibility of the emergence of recombinant SARS-CoV-2. In fact, there are some reports showing the recombination between SARS-CoV-2 variants (Colson et al., 2022; Jackson et al., 2021; Lacek et al., 2022; Sekizuka et al., 2021), and particularly, the emergence of the BA.1-BA.2 recombinant, such as the Omicron XE variant, that harbors the BA.2 *S* gene has been recently reported (GitHub, 2022). Overall, the results of this study and others indicate that it might be possible for certain recombinants to emerge that harbor the BA.2 *S* gene in a non-BA.2 genomic backbone, which can exhibit higher pathogenicity, as shown in this study.

STAR★METHODS

Detailed methods are provided in the online version of this paper and include the following:

- KEY RESOURCES TABLE
- RESOURCE AVAILABILITY
  - Lead contact
  - Materials availability
  - Data and code availability
- EXPERIMENTAL MODEL AND SUBJECT DETAILS
  - Ethics statement
  - Human serum collection
  - Cell culture
- METHOD DETAILS
  - Viral genome sequencing
  - Phylogenetic and comparative genome analyses
  - Modeling the epidemic dynamics of SARS-CoV-2 lineages
  - Plasmid construction
  - Preparation of monoclonal antibodies
  - Preparation of mouse sera
  - Neutralization assay
  - SARS-CoV-2 reverse genetics
  - SARS-CoV-2 preparation and titration
  - SARS-CoV-2 infection
  - RT–qPCR
  - Fluorescence microscopy
  - Plaque assay
  - Coculture experiment
  - SARS-CoV-2 S-based fusion assay
  - Western blot
  - Pseudovirus infection
  - Yeast surface display
  - TMPRSS2 expression on the cell surface
  - E64d treatment
  - Cytotoxicity assay
  - Animal experiments
  - Lung function test
  - IHC
  - H&E staining
  - Histopathological scoring
- QUANTIFICATION AND STATISTICAL ANALYSIS

SUPPLEMENTAL INFORMATION

Supplemental information can be found online at https://doi.org/10.1016/j.cell.2022.04.035.

CONSORTIA

The Genotype to Phenotype Japan (G2P-Japan) Consortium: Mai Suganami, Akiko Oide, Mika Chiba, Tomokazu Tamura, Kana Tsushima, Haruko Kubo, Zannatul Ferdous, Hiromi Mouri, Miki Iida, Keiko Kasahara, Koshiro Tabata, Mariko Ishizuka, Asako Shigeno, Kenzo Tokunaga, Seiya Ozono, Isao Yoshida, So Nakagawa, Jiaqi Wu, Miyoko Takahashi, Bahityar Rahmutulla Nawai, Yutaka Suzuki, Yasuhiro Kazuma, Ryosuke Nomura, Yoshihito Horisawa, Yusuke Tashiro, Yohei Yanagida, Yugo Kawai, Ryoko Kawabata, Otowa Takahashi, Kimiko Ichihara, Kazuko Kitazato, Haruyo Hasebe, Chihiro Motozono, Toong Seng Tan, and Isaac Ngare.

ACKNOWLEDGMENTS

We would like to thank all members belonging to The Genotype to Phenotype Japan (G2P-Japan) Consortium. We thank Dr. Kenzo Tokunaga (National Institute for Infectious Diseases, Japan) and Dr. Jin Gohda (the University of Tokyo, Japan) and Dr. Hisashi Arase (Osaka University) for providing reagents. We gratefully acknowledge the laboratories responsible for obtaining the specimens and the laboratories where genetic sequence data were generated and shared via the GISAID Initiative. A full list of originating and submitting laboratories for the sequences used in our analysis can be found at https://www.gisaid.org using the EPI-SET-ID: EPI_SET_20220511qk. The supercomputing resource was provided by Human Genome Center at the University of Tokyo.

This study was supported in part by AMED Research Program on Emerging and Re-emerging Infectious Diseases (20fk0108268 to A.T.-K.; 20fk0108517 to A.T.-K.; 20fk0108401 to T.F.; 20fk010847 to T.F.; 21fk0108617 to T.F.; 20fk0108146 to K. Sato; 20fk0108270 to K. Sato; and 20fk0108413 to A.K., T. Ikeda, and K. Sato) and 20fk0108451 to G2P-Japan Consortium, A.S., T. Irie, K.M., T.F., T. Ikeda, and K. Sato; AMED Research Program on HIV/AIDS (21fk0410034 to A.T.-K.; 21fk0410033 to A.S.; and 21fk0410039 to K. Sato); AMED CRDF Global Grant (21jk0210039 to A.S.); AMED Japan Program for Infectious Diseases Research and Infrastructure (21wm0325009 to A.S.; 21wm0125008 to H.S. and 21wm0225003 to H.S.); JST A-STEP (JPMJTM20SL to T. Ikeda); JST SICORP (e-ASIA) (JPMJSC20U1 to K. Sato); JST SICORP (JPMJSC21U5 to K. Sato), JST CREST (JPMJCR20H4 to K. Sato); JSPS KAKENHI Grant-in-Aid for Scientific Research C (19K06382 to A.S.; 22K07103 to T. Ikeda); JSPS KAKENHI Grant-in-Aid for Scientific Research B (21H02736 to T.F.; 18H02662 to K. Sato; and 21H02737 to K. Sato); JSPS KAKENHI Grant-in-Aid for Early-Career Scientists (22K16375 to H.N.; 20K15767 J.I.); JSPS Fund for the Promotion of Joint International Research (Fostering Joint International Research) (18KK0447 to K. Sato); JSPS Core-to-Core Program (A. Advanced Research Networks) (JPJSCCA20190008 to K. Sato); JSPS Research Fellow DC1 (19J20488 to I.K.); JSPS Leading Initiative for Excellent Young Researchers (LEADER) (to T. Ikeda); World-leading Innovative and Smart Education (WISE) Program 1801 from the Ministry of Education, Culture, Sports, Science and Technology (MEXT) (to N.N.); the Tokyo Biochemical Research Foundation (to K. Sato); Mitsubishi Foundation (to T. Ikeda); Shin-Nihon Foundation of Advanced Medical Publishing Research (to M.T. and T. Ikeda); Tsuchiya Foundation (to T. Irie); a Grant for Joint Research Projects of the Research Institute for Microbial Diseases, Osaka University (to A.S.); an intramural grant from Kumamoto University COVID-19 Research Projects (AMABIE) (to T. Ikeda); Intercontinental Research and Educational Platform Aiming for Eradication of HIV/AIDS (to T. Ikeda); and Joint Usage/Research Center program of Institute for Frontier Life and Medical Sciences, Kyoto University (to K. Sato).

AUTHOR CONTRIBUTIONS

D.Y., I.K., H.N., K.U., K. Shirakawa, Y.K., M. Toyoda, Y.L.T., E.P.B., R.S., K.N., T.U., A.S., T. Irie, T. Ikeda, and K. Sato performed cell culture experiments. J.Z. and G.S. performed a yeast surface display assay. Y.M., N.N., R.S., M.K., K.K.,

T.H., H.I., Y. Orba, M. Sasaki, K. Yoshimatsu, K.J.I., H.S., K.M., and T.F. performed animal experiments. M. Tsuda, L.W., Y. Oda, and S.T. performed histopathological analysis. H.A., M.N., K. Sadamasu, and K. Yoshimura performed viral genome sequencing analysis. K. Shirakawa, J.K., M. Seki, R.F., A.K., T.S., T-a.N., S.S., T.S., and A.T.-K. contributed clinical sample collection. J.I. performed statistical, modeling, and bioinformatics analyses. J.I., A.S., T. Irie, S.T., K.M., T.F., T. Ikeda, and K. Sato designed the experiments and interpreted the results. J.I. and K. Sato wrote the original manuscript. All authors reviewed and proofread the manuscript. The Genotype to Phenotype Japan (G2P-Japan) Consortium contributed to the project administration.

DECLARATION OF INTERESTS

The authors declare no competing interests.

Received: February 24, 2022
Revised: March 24, 2022
Accepted: April 26, 2022
Published: May 2, 2022

REFERENCES

Bouckaert, R., Heled, J., Kühnert, D., Vaughan, T., Wu, C.H., Xie, D., Suchard, M.A., Rambaut, A., and Drummond, A.J. (2014). BEAST 2: a software platform for Bayesian evolutionary analysis. PLoS Comput. Biol. *10*, e1003537. https://doi.org/10.1371/journal.pcbi.1003537.

Cameroni, E., Bowen, J.E., Rosen, L.E., Saliba, C., Zepeda, S.K., Culap, K., Pinto, D., VanBlargan, L.A., De Marco, A., di Iulio, J., et al. (2022). Broadly neutralizing antibodies overcome SARS-CoV-2 Omicron antigenic shift. Nature *602*, 664–670. https://doi.org/10.1038/s41586-021-04386-2.

Cao, Y., Wang, J., Jian, F., Xiao, T., Song, W., Yisimayi, A., Huang, W., Li, Q., Wang, P., An, R., et al. (2021). Omicron escapes the majority of existing SARS-CoV-2 neutralizing antibodies. Nature *602*, 657–663. https://doi.org/10.1038/d41586-41021-03796-41586.

Capella-Gutiérrez, S., Silla-Martínez, J.M., and Gabaldón, T. (2009). trimAl: a tool for automated alignment trimming in large-scale phylogenetic analyses. Bioinformatics *25*, 1972–1973. https://doi.org/10.1093/bioinformatics/btp348.

Cele, S., Jackson, L., Khoury, D.S., Khan, K., Moyo-Gwete, T., Tegally, H., San, J.E., Cromer, D., Scheepers, C., Amoako, D., et al. (2021). Omicron extensively but incompletely escapes Pfizer BNT162b2 neutralization. Nature *602*, 654–656. https://doi.org/10.1038/d41586-41021-03824-41585.

Chen, S., Zhou, Y., Chen, Y., and Gu, J. (2018). Fastp: an ultra-fast all-in-one FASTQ preprocessor. Bioinformatics *34*, i884–i890. https://doi.org/10.1093/bioinformatics/bty560.

Cingolani, P., Platts, A., Wang, le L., Coon, M., Nguyen, T., Wang, L., Land, S.J., Lu, X., and Ruden, D.M. (2012). A program for annotating and predicting the effects of single nucleotide polymorphisms, SnpEff: SNPs in the genome of Drosophila melanogaster strain w1118; iso-2; iso-3. Fly (Austin) *6*, 80–92. https://doi.org/10.4161/fly.19695.

Colson, P., Fournier, P.-E., Delerce, J., Million, M., Bedotto, M., Houhamdi, L., Yahi, N., Bayette, J., Levasseur, A., Fantini, J., et al. (2022). Culture and identification of a Deltamicron SARS-CoV-2 in a three cases cluster in southern France. MedRxiv. https://doi.org/10.1101/2022.1103.1103.22271812.

Dejnirattisai, W., Huo, J., Zhou, D., Zahradník, J., Supasa, P., Liu, C., Duyvesteyn, H.M.E., Ginn, H.M., Mentzer, A.J., Tuekprakhon, A., et al. (2022). SARS-CoV-2 Omicron-B.1.1.529 leads to widespread escape from neutralizing antibody responses. Cell *185*, 467–484.e15. https://doi.org/10.1016/j.cell.2021.12.046.

Dejnirattisai, W., Shaw, R.H., Supasa, P., Liu, C., Stuart, A.S., Pollard, A.J., Liu, X., Lambe, T., Crook, D., Stuart, D.I., et al. (2021). Reduced neutralisation of SARS-CoV-2 omicron B.1.1.529 variant by post-immunisation serum. Lancet *399*, 234–236. https://doi.org/10.1016/S0140-6736(1021)02844-02840.

Ferreira, I.A.T.M., Kemp, S.A., Datir, R., Saito, A., Meng, B., Rakshit, P., Takaori-Kondo, A., Kosugi, Y., Uriu, K., Kimura, I., et al. (2021). SARS-CoV-2 B.1.617 Mutations L452R and E484Q are not synergistic for antibody evasion. J. Infect. Dis. *224*, 989–999. https://doi.org/10.1093/infdis/jiab368.

Garcia-Beltran, W.F., Denis, K.J.S., Hoelzemer, A., Lam, E.C., Nitido, A.D., Sheehan, M.L., Berrios, C., Ofoman, O., Chang, C.C., Hauser, B.M., et al. (2021). mRNA-based COVID-19 vaccine boosters induce neutralizing immunity against SARS-CoV-2 Omicron variant. Cell *185*, 457–466.e4. https://doi.org/10.1016/j.cell.2021.1012.1033.

Halfmann, P.J., Iida, S., Iwatsuki-Horimoto, K., Maemura, T., Kiso, M., Scheaffer, S.M., Darling, T.L., Joshi, A., Loeber, S., Singh, G., et al. (2022). SARS-CoV-2 Omicron virus causes attenuated disease in mice and hamsters. Nature *603*, 687–692. https://doi.org/10.1038/s41586-022-04441-6.

Han, P., Li, L., Liu, S., Wang, Q., Zhang, D., Xu, Z., Han, P., Li, X., Peng, Q., Su, C., et al. (2022). Receptor binding and complex structures of human ACE2 to spike RBD from omicron and delta SARS-CoV-2. Cell *185*, 630–640.e10. https://doi.org/10.1016/j.cell.2022.01.001.

Hasegawa, M., Kishino, H., and Yano, T. (1985). Dating of the human-ape splitting by a molecular clock of mitochondrial DNA. J. Mol. Evol. *22*, 160–174. https://doi.org/10.1007/BF02101694.

HKSAR (2022). Coronavirus disease (COVID-19) in HK (March 18, 2022). https://chp-dashboard.geodata.gov.hk/covid-19/en.html.

Hoffmann, M., Kleine-Weber, H., Schroeder, S., Krüger, N., Herrler, T., Erichsen, S., Schiergens, T.S., Herrler, G., Wu, N.H., Nitsche, A., et al. (2020). SARS-CoV-2 cell entry depends on ACE2 and TMPRSS2 and is blocked by a clinically proven protease inhibitor. Cell *181*, 271–280.e8. https://doi.org/10.1016/j.cell.2020.02.052.

Ito, K., Piantham, C., and Nishiura, H. (2022). Estimating relative generation times and relative reproduction numbers of Omicron BA.1 and BA.2 with respect to Delta in Denmark. MedRxiv. https://doi.org/10.1101/2022.1103.1102.22271767.

Jackson, B., Boni, M.F., Bull, M.J., Colleran, A., Colquhoun, R.M., Darby, A.C., Haldenby, S., Hill, V., Lucaci, A., McCrone, J.T., et al. (2021). Generation and transmission of interlineage recombinants in the SARS-CoV-2 pandemic. Cell *184*, 5179–5188.e8. https://doi.org/10.1016/j.cell.2021.08.014.

Kawaoka, Y., Uraki, R., Kiso, M., Iida, S., Imai, M., Takashita, E., Kuroda, M., Halfmann, P., Loeber, S., Maemura, T., et al. (2022). Characterization and antiviral susceptibility of SARS-CoV-2 Omicron/BA.2. Res. Sq.

Khare, S., Gurry, C., Freitas, L., Schultz, M.B., Bach, G., Diallo, A., Akite, N., Ho, J., Lee, R.T., Yeo, W., et al. (2021). GISAID's role in pandemic response. China CDC Wkly. *3*, 1049–1051. https://doi.org/10.46234/ccdcw2021.255.

Kimura, I., Kosugi, Y., Wu, J., Zahradnik, J., Yamasoba, D., Butlertanaka, E.P., Tanaka, Y.L., Uriu, K., Liu, Y., Morizako, N., et al. (2022). The SARS-CoV-2 Lambda variant exhibits enhanced infectivity and immune resistance. Cell Rep. *38*, 110218. https://doi.org/10.1016/j.celrep.2021.110218.

Kondo, N., Miyauchi, K., and Matsuda, Z. (2011). Monitoring viral-mediated membrane fusion using fluorescent reporter methods. Curr. Protoc. Cell Biol. *Chapter 26*, Unit 26.9. https://doi.org/10.1002/0471143030.cb2609s50.

Lacek, K.A., Rambo-Martin, B., Batra, D., Zheng, X.-y., Keller, M.W., Wilson, M., Sheth, M., Davis, M., Burroughs, M., Gerhart, J., et al. (2022). Genome recombination between delta and alpha variants of severe acute respiratory syndrome coronavirus 2 (SARS-CoV-2). MedRxiv. https://doi.org/10.1101/2022.1103.1119.484981.

Li, H. (2018). Minimap2: pairwise alignment for nucleotide sequences. Bioinformatics *34*, 3094–3100. https://doi.org/10.1093/bioinformatics/bty191.

Li, H., and Durbin, R. (2009). Fast and accurate short read alignment with Burrows-Wheeler transform. Bioinformatics *25*, 1754–1760. https://doi.org/10.1093/bioinformatics/btp324.

Li, H., Handsaker, B., Wysoker, A., Fennell, T., Ruan, J., Homer, N., Marth, G., Abecasis, G., and Durbin, R.; 1000 Genome Project Data Processing Subgroup (2009). The sequence alignment/map format and SAMtools. Bioinformatics *25*, 2078–2079. https://doi.org/10.1093/bioinformatics/btp352.

Liu, L., Iketani, S., Guo, Y., Chan, J.F.-W., Wang, M., Liu, L., Luo, Y., Chu, H., Huang, Y., Nair, M.S., et al. (2021a). Striking antibody evasion manifested by

the Omicron variant of SARS-CoV-2. Nature *602*, 676–681. https://doi.org/10.1038/d41586-41021-03826-41583.

Liu, Y., Arase, N., Kishikawa, J.-i., Hirose, M., Li, S., Tada, A., Matsuoka, S., Arakawa, A., Akamatsu, K., Ono, C., et al. (2021b). The SARS-CoV-2 Delta variant is poised to acquire complete resistance to wild-type spike vaccines. bioRxiv. https://doi.org/10.1101/2021.1108.1122.457114.

Matsuyama, S., Nao, N., Shirato, K., Kawase, M., Saito, S., Takayama, I., Nagata, N., Sekizuka, T., Katoh, H., Kato, F., et al. (2020). Enhanced isolation of SARS-CoV-2 by TMPRSS2-expressing cells. Proc. Natl. Acad. Sci. USA *117*, 7001–7003. https://doi.org/10.1073/pnas.2002589117.

Meng, B., Abdullahi, A., Ferreira, I.A.T.M., Goonawardane, N., Saito, A., Kimura, I., Yamasoba, D., Gerber, P.P., Fatihi, S., Rathore, S., et al. (2022). Altered TMPRSS2 usage by SARS-CoV-2 Omicron impacts infectivity and fusogenicity. Nature *603*, 706–714. https://doi.org/10.1038/s41586-022-04474-x.

Mlcochova, P., Kemp, S.A., Dhar, M.S., Papa, G., Meng, B., Ferreira, I.A.T.M., Datir, R., Collier, D.A., Albecka, A., Singh, S., et al. (2021). SARS-CoV-2 B.1.617.2 Delta variant replication and immune evasion. Nature *599*, 114–119. https://doi.org/10.1038/s41586-021-03944-y.

Motozono, C., Toyoda, M., Zahradnik, J., Saito, A., Nasser, H., Tan, T.S., Ngare, I., Kimura, I., Uriu, K., Kosugi, Y., et al. (2021). SARS-CoV-2 spike L452R variant evades cellular immunity and increases infectivity. Cell Host Microbe *29*, 1124–1136.e11. https://doi.org/10.1016/j.chom.2021.06.006.

Niwa, H., Yamamura, K., and Miyazaki, J. (1991). Efficient selection for high-expression transfectants with a novel eukaryotic vector. Gene *108*, 193–199. https://doi.org/10.1016/0378-1119(91)90434-d.

Obermeyer, F., Schaffner, S.F., Jankowiak, M., Barkas, N., Pyle, J.D., Park, D.J., MacInnis, B.L., Luban, J., Sabeti, P.C., and Lemieux, J.E. (2022). Analysis of 2.1 million SARS-CoV-2 genomes identifies mutations associated with transmissibility. MedRxiv. https://doi.org/10.1101/2021.1109.1107.21263228.

Ozono, S., Zhang, Y., Ode, H., Sano, K., Tan, T.S., Imai, K., Miyoshi, K., Kishigami, S., Ueno, T., Iwatani, Y., et al. (2021). SARS-CoV-2 D614G spike mutation increases entry efficiency with enhanced ACE2-binding affinity. Nat. Commun. *12*, 848. https://doi.org/10.1038/s41467-021-21118-2.

Ozono, S., Zhang, Y., Tobiume, M., Kishigami, S., and Tokunaga, K. (2020). Super-rapid quantitation of the production of HIV-1 harboring a luminescent peptide tag. J. Biol. Chem. *295*, 13023–13030. https://doi.org/10.1074/jbc.RA120.013887.

Peleg, Y., and Unger, T. (2014). Application of the restriction-free (RF) cloning for multicomponents assembly. Methods Mol. Biol. *1116*, 73–87. https://doi.org/10.1007/978-1-62703-764-8_6.

Planas, D., Saunders, N., Maes, P., Guivel-Benhassine, F., Planchais, C., Buchrieser, J., Bolland, W.-H., Porrot, F., Staropoli, I., Lemoine, F., et al. (2021). Considerable escape of SARS-CoV-2 Omicron to antibody neutralization. Nature *602*, 671–675. https://doi.org/10.1038/d41586-41021-03827-41582.

GitHub (2022). Potential BA.1/BA.2 recombinant lineage with likely breakpoint at NSP5/NSP6 (267 sequences in the UK and Ireland. https://github.com/cov-lineages/pango-designation/issues/454.

Qassim, S.H., Chemaitelly, H., Ayoub, H.H., AlMukdad, S., Tang, P., Hasan, M.R., Yassine, H.M., Al-Khatib, H.A., Smatti, M.K., Abdul-Rahim, H.F., et al. (2022). Effects of BA.1/BA.2 subvariant, vaccination, and prior infection on infectiousness of SARS-CoV-2 Omicron infections. MedRxiv. https://doi.org/10.1101/2022.1103.1102.22271771.

Reed, L.J., and Muench, H. (1938). A simple method of estimating fifty percent endpoints. Am. J. Hyg. *27*, 493–497.

Saito, A., Irie, T., Suzuki, R., Maemura, T., Nasser, H., Uriu, K., Kosugi, Y., Shirakawa, K., Sadamasu, K., Kimura, I., et al. (2022). Enhanced fusogenicity and pathogenicity of SARS-CoV-2 Delta P681R mutation. Nature *602*, 300–306. https://doi.org/10.1038/s41586-021-04266-9.

Schubert, M., Bertoglio, F., Steinke, S., Heine, P.A., Ynga-Durand, M.A., Maass, H., Sammartino, J.C., Cassaniti, I., Zuo, F., Du, L., et al. (2022). Human serum from SARS-CoV-2 vaccinated and COVID-19 patients shows reduced binding to the RBD of SARS-CoV-2 Omicron variant. BMC Med. *20 102*. https://doi.org/10.1101/2021.1112.1110.21267523.

Sekizuka, T., Itokawa, K., Saito, M., Shimatani, M., Matsuyama, S., Hasegawa, H., and Saito, T.; COVID-19 Genomic Surveillance Network in Japan (COG-JP) (2021). Genome recombination between Delta and Alpha variants of severe acute respiratory syndrome coronavirus 2 (SARS-CoV-2). MedRxiv. https://doi.org/10.1101/2021.1110.1111.21264606.

Shuai, H., Chan, J.F., Hu, B., Chai, Y., Yuen, T.T., Yin, F., Huang, X., Yoon, C., Hu, J.C., Liu, H., et al. (2022). Attenuated replication and pathogenicity of SARS-CoV-2 B.1.1.529 Omicron. Nature *603*, 693–699. https://doi.org/10.1038/s41586-022-04442-5.

Stamatakis, A. (2014). RAxML version 8: a tool for phylogenetic analysis and post-analysis of large phylogenies. Bioinformatics *30*, 1312–1313. https://doi.org/10.1093/bioinformatics/btu033.

Suzuki, R., Yamasoba, D., Kimura, I., Wang, L., Kishimoto, M., Ito, J., Morioka, Y., Nao, N., Nasser, H., Uriu, K., et al. (2022). Attenuated fusogenicity and pathogenicity of SARS-CoV-2 Omicron variant. Nature *603*, 700–705. https://doi.org/10.1038/s41586-022-04462-1.

Takashita, E., Kinoshita, N., Yamayoshi, S., Sakai-Tagawa, Y., Fujisaki, S., Ito, M., Iwatsuki-Horimoto, K., Chiba, S., Halfmann, P., Nagai, H., et al. (2022). Efficacy of antibodies and antiviral drugs against Covid-19 Omicron variant. N. Engl. J. Med. *386*, 995–998. https://doi.org/10.1056/NEJMc2119407.

Torii, S., Ono, C., Suzuki, R., Morioka, Y., Anzai, I., Fauzyah, Y., Maeda, Y., Kamitani, W., Fukuhara, T., and Matsuura, Y. (2021). Establishment of a reverse genetics system for SARS-CoV-2 using circular polymerase extension reaction. Cell Rep. *35*, 109014.

UKHSA (2022). SARS-CoV-2 variants of concern and variants under investigation in England. Tech. Briefing *35*. https://assets.publishing.service.gov.uk/government/uploads/system/uploads/attachment_data/file/1050999/Technical-Briefing-35-28January2022.pdf.

Uriu, K., Kimura, I., Shirakawa, K., Takaori-Kondo, A., Nakada, T.A., Kaneda, A., Nakagawa, S., and Sato, K.; The Genotype to Phenotype Japan (G2P-Japan) (2021). Neutralization of the SARS-CoV-2 Mu variant by convalescent and vaccine serum. N. Engl. J. Med. *385*, 2397–2399. https://doi.org/10.1056/NEJMc2114706.

VanBlargan, L.A., Errico, J.M., Halfmann, P.J., Zost, S.J., Crowe, J.E., Jr., Purcell, L.A., Kawaoka, Y., Corti, D., Fremont, D.H., and Diamond, M.S. (2022). An infectious SARS-CoV-2 B.1.1.529 Omicron virus escapes neutralization by therapeutic monoclonal antibodies. Nat. Med. *28*, 490–495. https://doi.org/10.1038/s41591-021-01678-y.

Viana, R., Moyo, S., Amoako, D.G., Tegally, H., Scheepers, C., Althaus, C.L., Anyaneji, U.J., Bester, P.A., Boni, M.F., Chand, M., et al. (2022). Rapid epidemic expansion of the SARS-CoV-2 Omicron variant in southern Africa. Nature *603*, 679–686. https://doi.org/10.1038/s41586-022-04411-y.

V'Kovski, P., Kratzel, A., Steiner, S., Stalder, H., and Thiel, V. (2021). Coronavirus biology and replication: implications for SARS-CoV-2. Nat. Rev. Microbiol. *19*, 155–170. https://doi.org/10.1038/s41579-020-00468-6.

Vöhringer, H.S., Sanderson, T., Sinnott, M., De Maio, N., Nguyen, T., Goater, R., Schwach, F., Harrison, I., Hellewell, J., Ariani, C.V., et al. (2021). Genomic reconstruction of the SARS-CoV-2 epidemic in England. Nature *600*, 506–511. https://doi.org/10.1038/s41586-021-04069-y.

WHO (2021). Classification of Omicron (B.1.1.529): SARS-CoV-2 variant of concern (November 26, 2021). https://www.who.int/news/item/26-11-2021-classification-of-omicron-(b.1.1.529)-sars-cov-2-variant-of-concern.

WHO (2022). Tracking SARS-CoV-2 variants (February 3, 2022). https://www.who.int/en/activities/tracking-SARS-CoV-2-variants/.

Wolter, N., Jassat, W., Gottberg, A.v., and Cohen, C. (2022). Clinical severity of Omicron sub-lineage BA.2 compared to BA.1 in South Africa. MedRxiv. https://doi.org/10.1101/2022.1102.1117.22271030.

Wu, F., Zhao, S., Yu, B., Chen, Y.M., Wang, W., Song, Z.G., Hu, Y., Tao, Z.W., Tian, J.H., Pei, Y.Y., et al. (2020). A new coronavirus associated with human respiratory disease in China. Nature *579*, 265–269. https://doi.org/10.1038/s41586-020-2008-3.

Wu, L., Zhou, L., Mo, M., Liu, T., Wu, C., Gong, C., Lu, K., Gong, L., Zhu, W., and Xu, Z. (2022). SARS-CoV-2 Omicron RBD shows weaker binding affinity than the currently dominant Delta variant to human ACE2. Signal Transduct. Target. Ther. *7*, 8. https://doi.org/10.1038/s41392-021-00863-2.

Yamamoto, M., Kiso, M., Sakai-Tagawa, Y., Iwatsuki-Horimoto, K., Imai, M., Takeda, M., Kinoshita, N., Ohmagari, N., Gohda, J., Semba, K., et al. (2020). The anticoagulant nafamostat potently inhibits SARS-CoV-2 S protein-mediated fusion in a cell fusion assay system and viral infection in vitro in a cell-type-dependent manner. Viruses *12*, 629. https://doi.org/10.3390/v12060629.

Zahradník, J., Dey, D., Marciano, S., Kolářová, L., Charendoff, C.I., Subtil, A., and Schreiber, G. (2021a). A protein-engineered, enhanced yeast display platform for rapid evolution of challenging targets. ACS Synth. Biol. *10*, 3445–3460. https://doi.org/10.1021/acssynbio.1c00395.

Zahradník, J., Marciano, S., Shemesh, M., Zoler, E., Harari, D., Chiaravalli, J., Meyer, B., Rudich, Y., Li, C., Marton, I., et al. (2021b). SARS-CoV-2 variant prediction and antiviral drug design are enabled by RBD in vitro evolution. Nat. Microbiol. *6*, 1188–1198. https://doi.org/10.1038/s41564-021-00954-4.

Zhao, M.M., Yang, W.L., Yang, F.Y., Zhang, L., Huang, W.J., Hou, W., Fan, C.F., Jin, R.H., Feng, Y.M., Wang, Y.C., et al. (2021). Cathepsin L plays a key role in SARS-CoV-2 infection in humans and humanized mice and is a promising target for new drug development. Signal Transduct. Target. Ther. *6*, 134. https://doi.org/10.1038/s41392-021-00558-8.

STAR★METHODS

KEY RESOURCES TABLE

REAGENT or RESOURCE	SOURCE	IDENTIFIER
Antibodies		
Casirivimab	This study	N/A
Imdevimab	This study	N/A
Sotrovimab	This study	N/A
Rabbit anti-SARS-CoV-2 S S1/S2 polyclonal antibody	Thermo Fisher Scientific	Cat# PA5-112048; RRID: AB_2866784
Normal rabbit IgG	Southern Biotech	Cat# 0111-01; RRID: AB_2732899
APC-conjugated goat anti-rabbit IgG polyclonal antibody	Jackson ImmunoResearch	Cat# 111-136-144; RRID: AB_2337987
Mouse anti-SARS-CoV-2 S monoclonal antibody (clone 1A9)	GeneTex	Cat# GTX632604; RRID: AB_2864418
Mouse anti-HIV-1 p24 monoclonal antibody (clone 183-H12-5C)	NIH HIV Reagent Program	Cat# ARP-3537; RRID: AB_2819250
Rabbit anti-beta actin (ACTB) monoclonal antibody (clone 13E5)	Cell Signaling	Cat# 4970; RRID: AB_2223172
HRP-conjugated donkey anti-rabbit IgG polyclonal antibody	Jackson ImmunoResearch	Cat# 711-035-152; RRID: AB_10015282
HRP-conjugated donkey anti-mouse IgG polyclonal antibody	Jackson ImmunoResearch	Cat# 715-035-150; RRID: AB_2340770
Rabbit anti-TMPRSS2 polyclonal antibody	BIOSS	Cat# BS-6285R; RRID: AB_11102333
Mouse anti-SARS-CoV-2 N monoclonal antibody (clone 1035111)	R&D systems	Cat# MAB10474-SP; RRID: N/A
Bacterial and virus strains		
SARS-CoV-2 (strain WK-521, A lineage)	(Matsuyama et al., 2020)	GISAID ID: EPI_ISL_408667
Recombinant SARS-CoV-2, rB.1.1 S-GFP	(Saito et al., 2022)	N/A
Recombinant SARS-CoV-2, rDelta S-GFP	This study	N/A
Recombinant SARS-CoV-2, rBA.1 S-GFP	This study	N/A
Recombinant SARS-CoV-2, rBA.2 S-GFP	This study	N/A
Biological samples		
Human sera	This study	N/A
Primary human nasal epithelial cells	Epithelix	Cat# EP02, Batch# MP0010
Chemicals, peptides, and recombinant proteins		
Fetal bovine serum	Sigma-Aldrich	Cat# 172012-500ML
Penicillin-streptomycin	Sigma-Aldrich	Cat# P4333-100ML
DMEM (high glucose)	Sigma-Aldrich	Cat# 6429-500ML
DMEM (low glucose)	Wako	Cat# 041-29775
EMEM	Wako	Cat# 051-07615
EMEM	Sigma-Aldrich	Cat# M4655-500ML
EMEM	Wako	Cat# 056-08385
Expi293 expression medium	Thermo Fisher Scientific	Cat# A1435101
Puromycin	InvivoGen	Cat# ant-pr-1
Hygromycin	Nacalai Tesque	Cat# 09287-84
Blasticidin	InvivoGen	Cat# ant-bl-1
G418	Nacalai Tesque	Cat# G8168-10ML
KpnI	New England Biolab	Cat# R0142S
NotI	New England Biolab	Cat# R1089S

(*Continued on next page*)

Continued

REAGENT or RESOURCE	SOURCE	IDENTIFIER
PEI Max	Polysciences	Cat# 24765-1
Complete Freund's adjuvant	Sigma-Aldrich	Cat# F5881
TransIT-LT1	Takara	Cat# MIR2300
Doxycycline	Takara	Cat# 1311N
TURBO DNase	Thermo Fisher Scientific	Cat# AM2238
Opti-MEM	Thermo Fisher Scientific	Cat# 11058021
Triton X-100	Nacalai Tesque	Cat# 35501-15
Recombinant RNase inhibitor	Takara	Cat# 2313B
Carboxymethyl cellulose	Wako	Cat# 039-01335
4% Paraformaldehyde in PBS	Nacalai Tesque	Cat# 09154-85
Methylene blue	Nacalai Tesque	Cat# 22412-14
Poly-L-lysine	Sigma	Cat# P4832
Hoechst 33342	Thermo Fisher Scientific	Cat# H3570
Fluoromount-G	Southern Biotech	Cat# 0100-01
EnduRen live cell substrate	Promega	Cat# E6481
Nonidet P40 substitute	Nacalai Tesque	Cat# 18558-54
Protease inhibitor cocktail	Nacalai Tesque	Cat# 03969-21
Protein assay dye	Bio-Rad	Cat# 5000006
1× NuPAGE LDS sample buffer	Thermo Fisher Scientific	Cat# NP0007
SuperSignal west femto maximum sensitivity substrate	Thermo Fisher Scientific	Cat# 34095
Soluble human ACE2 (residues 18-740)	This study	N/A
CF640	Biotium	Cat# 9210
SARS-CoV-2 B.1.1 RBD	(Kimura et al., 2022; Motozono et al., 2021)	N/A
SARS-CoV-2 BA.1 RBD	(Dejnirattisai et al., 2022)	N/A
SARS-CoV-2 BA.2 RBD	This study	N/A
Bilirubin	Sigma-Aldrich	Cat# 14370–1G
E64d (Aloxistatin)	Selleck	Cat# S7393
Medetomidine hydrochloride (Domitor®)	Nippon Zenyaku Kogyo	N/A
Midazolam	FUJIFILM Wako Chemicals	Cat# 135–13791
Butorphanol (Vetorphale®)	Meiji Seika Pharma	N/A
Alphaxaone (Alfaxan®)	Jurox	N/A
Isoflurane	Sumitomo Dainippon Pharma	N/A
EnVision FLEX target retrieval solution high pH	Agilent	Cat# K8004
Critical commercial assays		
QIAamp viral RNA mini kit	Qiagen	Cat# 52906
NEB next ultra RNA library prep kit for Illumina	New England Biolabs	Cat# E7530
MiSeq reagent kit v3	Illumina	Cat# MS-102-3001
NAb protein A plus spin kit	Thermo Fisher Scientific	Cat# 89948
One Step TB Green PrimeScript PLUS RT-PCR kit	Takara	Cat# RR096A
SARS-CoV-2 direct detection RT-qPCR kit	Takara	Cat# RC300A
Nano Glo HiBiT lytic detection system	Promega	Cat# N3040
ACE2 activity assay kit	SensoLyte	Cat# AS-72086
KAPA HiFi HotStart ReadyMix kit	Roche	Cat# KK2601
Bright-Glo luciferase assay system	Promega	Cat# E2620
Cell counting kit-8	Dojindo	Cat# CK04-11

(*Continued on next page*)

Continued

REAGENT or RESOURCE	SOURCE	IDENTIFIER
Deposited data		
Sequence data of recombinant SARS-CoV-2, working viruses	This study	GEO: GSE196649
Experimental models: Cell lines		
Human: HEK293T cells	ATCC	CRL-3216
Human: HEK293 cells	ATCC	CRL-1573
Human: HEK293-ACE2 cells	(Motozono et al., 2021)	N/A
Human: HEK293-ACE2/TMPRSS2 cells	(Motozono et al., 2021)	N/A
Human: HEK293-C34 cells	(Torii et al., 2021)	N/A
Human: HOS-ACE2/TMPRSS2 cells	(Ferreira et al., 2021; Ozono et al., 2021)	N/A
African green monkey (*Chlorocebus sabaeus*): Vero cells	JCRB Cell Bank	JCRB0111
African green monkey (*Chlorocebus sabaeus*): VeroE6/TMPRSS2 cells	JCRB Cell Bank	JCRB1819
Human: Calu-3 cells	ATCC	HTB-55
Human: Calu-3/DSP_{1-7} cells	(Yamamoto et al., 2020)	N/A
Mouse: B16F10 cells	RIKEN BioResource Research Center	RCB2630
Human: Expi293F cells	Thermo Fisher Scientific	Cat# A14527
Yeast (*Saccharomyces cerevisiae*): strain EBY100	ATCC	MYA-4941
Experimental models: Organisms/strains		
BALB/cCrSlc mice (female, 7 weeks old)	Japan SLC Inc.	http://www.jslc.co.jp/pdf/mouse/2020/004_BALB_cCrClc.pdf
Slc:Syrian hamsters (male, 4 weeks old)	Japan SLC Inc.	http://www.jslc.co.jp/pdf/hamster/2020/028_Slc_Syrian.pdf
Oligonucleotides		
Omi_ins214s-F1: TTC TAA GCA CAC GCC TAT TAT AGT GC	This study	N/A
Omi_ins214s-R1: TAA AGC CGA AAA ACC CTG AGG	This study	N/A
Omi_ins214s: FAM-TGA GCC AGA AGA TC-MGB	This study	N/A
Primers for the construction of pC-BA.2 S, see Table S3	This study	N/A
Primers for SARS-CoV-2 reverse genetics, see Table S3	This study	N/A
RT-qPCR, forward: AGC CTC TTC TCG TTC CTC ATC AC	This study	N/A
RT-qPCR, reverse: CCG CCA TTG CCA GCC ATT C	This study	N/A
Primers for the construction of yeast-optimized SARS-CoV-2 BA.2 RBD expression plasmid, see Table S3	This study	N/A
Recombinant DNA		
Plasmid: pC-B.1.1 S	(Motozono et al., 2021; Ozono et al., 2021)	N/A
Plasmid: pC-Alpha S	(Kimura et al., 2022)	N/A
Plasmid: pC-Delta S	(Kimura et al., 2022; Saito et al., 2022)	N/A
Plasmid: pC-BA.1 S	(Meng et al., 2022; Suzuki et al., 2022)	N/A
Plasmid: pC-BA.2 S	This study	N/A
Plasmid: pCAGGS	(Niwa et al., 1991)	N/A
Plasmid: psPAX2-IN/HiBiT	(Ozono et al., 2020)	N/A
Plasmid: pWPI-Luc2	(Ozono et al., 2020)	N/A
Plasmid: $pDSP_{1-7}$	(Kondo et al., 2011)	N/A
Plasmid: $pDSP_{8-11}$	(Kondo et al., 2011)	N/A
Plasmid: pC-ACE2	(Ozono et al., 2021)	N/A

(*Continued on next page*)

Continued

REAGENT or RESOURCE	SOURCE	IDENTIFIER
Plasmid: pC-TMPRSS2	(Ozono et al., 2021)	N/A
Plasmid: pJYDC1	Addgene	Cat# 162458
Software and algorithms		
fastp v0.21.0	(Chen et al., 2018)	https://github.com/OpenGene/fastp
BWA-MEM v0.7.17	(Li and Durbin, 2009)	http://bio-bwa.sourceforge.net
SAMtools v1.9	(Li et al., 2009)	http://www.htslib.org
snpEff v5.0e	(Cingolani et al., 2012)	http://pcingola.github.io/SnpEff
roblanf/sarscov2phylo: 13-11-20 (GISAID phylogenetic analysis pipeline)	GitHub,2022	https://github.com/roblanf/sarscov2phylo
Minimap2 v2.17	(Li, 2018)	https://github.com/lh3/minimap2
trimAl v1.2	(Capella-Gutiérrez et al., 2009)	http://trimal.cgenomics.org
RAxML v8.2.12	(Stamatakis, 2014)	https://cme.h-its.org/exelixis/web/software/raxml
BEAST2 v2.6.6	(Bouckaert et al., 2014)	https://www.beast2.org
CmdStan v2.28.1	The Stan Development Team	https://mc-stan.org
CmdStanr v0.4.0	The Stan Development Team	https://mc-stan.org/cmdstanr/
R v4.1.2	The R Foundation	https://www.r-project.org/
Sequencher v5.1 software	Gene Codes Corporation	N/A
In-house script	This study	https://github.com/TheSatoLab/Omicron_BA2/tree/main/lineage_growth_hierarchical_model
Prism 9 software v9.1.1	GraphPad Software	https://www.graphpad.com/scientific-software/prism/
BZ-X800 Analyzer v1.1.2.4	Keyence Corporation	N/A
Fiji software v2.2.0	ImageJ	https://fiji.sc
FlowJo software v10.7.1	BD Biosciences	https://www.flowjo.com/solutions/flowjo
Image Studio Lite v5.2	LI-COR Biosciences	N/A
Python v3.7	Python Software Foundation	https://www.python.org
FinePointe Station and Review softwares v2.9.2.12849	STARR	https://www.datasci.com/products/software/finepointe-software
NDP.scan software v3.2.4	Hamamatsu Photonics	https://nanozoomer.hamamatsu.com/jp/en/why_nanozoomer/scan.html
Other		
GISAID database	(Khare et al., 2021)	https://www.gisaid.org/
KEGG Drug Database	Kanehisa Laboratories	https://www.genome.jp/kegg/drug
BD microtainer blood collection tubes	BD Biosciences	Cat# 365967
5-ml HisTrap Fast Flow column	Cytiva	Cat# 17-5255-01
Superdex 200 16/600	Cytiva	Cat# 28-9893-35
3,3'-diaminobenzidine tetrahydrochloride	Dako	Cat# DM827
MAS-GP-coated glass slides	Matsunami Glass	Cat# S9901

RESOURCE AVAILABILITY

Lead contact

Further information and requests for resources and reagents should be directed to and will be fulfilled by the Lead Contact, Kei Sato (keisato@g.ecc.u-tokyo.ac.jp).

Materials availability

All unique reagents generated in this study are listed in the key resources table and available from the Lead Contact with a completed Materials Transfer Agreement.

Data and code availability

The raw data of virus sequences analyzed in this study are deposited in Gene Expression Omnibus (accession number: GSE196649). All databases/datasets used in this study are available from GISAID database (https://www.gisaid.org) and GenBank database (https://www.ncbi.nlm.nih.gov/genbank/). The accession numbers of viral sequences used in this study are listed in STARMethods.

The computational code to estimate the relative effective reproduction number of each viral lineage (Figure 1) is available in the GitHub repository (https://github.com/TheSatoLab/Omicron_BA2/tree/main/lineage_growth_hierarchical_model).

EXPERIMENTAL MODEL AND SUBJECT DETAILS

Ethics statement

All experiments with hamsters were performed in accordance with the Science Council of Japan's Guidelines for the Proper Conduct of Animal Experiments. The protocols were approved by the Institutional Animal Care and Use Committee of National University Corporation Hokkaido University (approval ID: 20-0123 and 20-0060). All experiments with mice were also performed in accordance with the Science Council of Japan's Guidelines for the Proper Conduct of Animal Experiments. The protocols were approved by the Institutional Animal Experiment Committee of The Institute of Medical Science, The University of Tokyo (approval ID: PA21-39). All protocols involving specimens from human subjects recruited at Kyoto University, Kuramochi Clinic Interpark and Chiba University were reviewed and approved by the Institutional Review Boards of Kyoto University (approval ID: G1309), Kuramochi Clinic Interpark (approval ID: G2021-004) and Chiba University (approval ID: HS202103-03). All human subjects provided written informed consent. All protocols for the use of human specimens were reviewed and approved by the Institutional Review Boards of The Institute of Medical Science, The University of Tokyo (approval IDs: 2021-1-0416 and 2021-18-0617), Kyoto University (approval ID: G0697), Kumamoto University (approval IDs: 2066 and 2074), and University of Miyazaki (approval ID: O-1021).

Human serum collection

Vaccine sera were collected from sixteen vaccinees four weeks after their second vaccination with the mRNA-1273 vaccine (Moderna) (average age: 27, range: 20-47, 38% male). Sera obtained from nine vaccinees 10-25 days after their second vaccination with the ChAdOx1 vaccine (Oxford-Astra Zeneca) (average age: 45, range: 35-54; 67% male) were purchased from BioIVT. Sera of thirteen individuals who had BNT162b2 vaccine (Pfizer/BioNTech) (average age: 37, range: 28-53; 54% male) were obtained at one month after the second dose, four months after the second dose, and one month after the third dose. The details of the vaccine sera are summarized in Table S2.

Convalescent sera were collected from vaccine-naïve individuals who had been infected with the alpha variant (n=8; average age: 41, range: 21-57, 63% male) or Delta variant (n=15; average age: 51, range: 22-67, 80% male). Convalescent sera of BA.1-infected individuals (n=21; average age: 40, range: 16-73; 48% male; 62% had received the second vaccination) were also collected. To identify the SARS-CoV-2 variants infecting patients, saliva was collected from COVID-19 patients during infection onset, and RNA was extracted using a QIAamp viral RNA mini kit (Qiagen, Cat# 52906) according to the manufacturer's protocol. To identified Alpha and Delta variants, viral genome sequencing was performed as previously described (Meng et al., 2022). For details, see the "Viral genome sequencing" section below. To identify the BA.1 variant, mutation-targeting RT–qPCR was performed. To identify the S E484A substitution (common in all Omicron variants including BA.1 and BA.2), an E484A (SARS-CoV-2) primer/probe set (Takara, Cat# RC322A) was used. To detect the S R214EPE insertion (specific to B.1.1.529 and BA.1, undetectable in BA.2), an in-house-developed protocol was used with the following primers and probe: Omi_ins214s-F1, 5'-TTC TAA GCA CAC GCC TAT TAT AGT GC-3'; Omi_ins214s-R1, 5'-TAA AGC CGA AAA ACC CTG AGG-3'; and Omi_ins214s, FAM-TGA GCC AGA AGA TC-MGB. Sera collected from twelve convalescents during the early pandemic (until May 2020) (average age: 71, range: 52-92, 8% male) were purchased from RayBiotech. Sera were inactivated at 56°C for 30 m and stored at –80°C until use. The details of the convalescent sera are summarized in Table S2.

Cell culture

HEK293T cells (a human embryonic kidney cell line; ATCC, CRL-3216), HEK293 cells (a human embryonic kidney cell line; ATCC, CRL-1573) and HOS-ACE2/TMPRSS2 cells, HOS cells stably expressing human ACE2 and TMPRSS2 (Ferreira et al., 2021; Ozono et al., 2021) were maintained in DMEM (high glucose) (Sigma-Aldrich, Cat# 6429-500ML) containing 10% fetal bovine serum (FBS, Sigma-Aldrich Cat# 172012-500ML), and 1% penicillin-streptomycin (PS) (Sigma-Aldrich, Cat# P4333-100ML). HEK293-ACE2 cells [HEK293 cells (ATCC, CRL-1573) stably expressing human ACE2] (Motozono et al., 2021) was maintained in DMEM (high glucose) containing 10% FBS, 1 μg/ml puromycin (InvivoGen, Cat# ant-pr-1) and 1% PS. HEK293-ACE2/TMPRSS2 cells [HEK293 cells (ATCC, CRL-1573) stably expressing human ACE2 and TMPRSS2] (Motozono et al., 2021) was maintained in DMEM (high glucose) containing 10% FBS, 1 μg/ml puromycin, 200 ng/ml hygromycin (Nacalai Tesque, Cat# 09287-84) and 1% PS. HEK293-C34 cells, *IFNAR1* KO HEK293 cells expressing human ACE2 and TMPRSS2 by doxycycline treatment (Torii et al., 2021), were maintained in DMEM (high glucose) containing 10% FBS, 10 μg/ml blasticidin (InvivoGen, Cat# ant-bl-1) and 1% PS. Vero cells [an African green monkey (*Chlorocebus sabaeus*) kidney cell line; JCRB Cell Bank, JCRB0111] were maintained in Eagle's minimum essential medium (EMEM) (Sigma-Aldrich, Cat# M4655-500ML) containing 10% FBS and 1% PS. VeroE6/TMPRSS2 cells (VeroE6 cells stably expressing human TMPRSS2; JCRB Cell Bank, JCRB1819) (Matsuyama et al., 2020) were maintained in DMEM (low glucose) (Wako, Cat#

041-29775) containing 10% FBS, G418 (1 mg/ml; Nacalai Tesque, Cat# G8168-10ML) and 1% PS. Calu-3 cells (a human lung epithelial cell line; ATCC, HTB-55) were maintained in EMEM (Sigma-Aldrich, Cat# M4655-500ML) containing 20% FBS and 1% PS. Calu-3/DSP_{1-7} cells [Calu-3 cells (ATCC, HTB-55) stably expressing DSP_{1-7}] (Yamamoto et al., 2020) were maintained in EMEM (Wako, Cat# 056-08385) supplemented with 20% FBS and 1% PS. B16F10 cells (a mouse melanoma cell line; RIKEN BioResource Research Center, RCB2630) were maintained in DMEM (high glucose) containing 10% FBS and 1% PS. Expi293F cells (Thermo Fisher Scientific, Cat# A14527) were maintained in Expi293 expression medium (Thermo Fisher Scientific, Cat# A1435101). Primary human nasal epithelial cells (Cat# EP02, Batch# MP0010) were purchased from Epithelix and maintained according to the manufacturer's procedure.

METHOD DETAILS

Viral genome sequencing

Viral genome sequencing was performed as previously described (Meng et al., 2022; Motozono et al., 2021; Saito et al., 2022; Suzuki et al., 2022) with some modifications. Briefly, the virus sequences were verified by viral RNA-sequencing analysis. Viral RNA was extracted using a QIAamp viral RNA mini kit (Qiagen, Cat# 52906). The sequencing library employed for total RNA sequencing was prepared using the NEB next ultra RNA library prep kit for Illumina (New England Biolabs, Cat# E7530). Paired-end 76-bp sequencing was performed using a MiSeq system (Illumina) with MiSeq reagent kit v3 (Illumina, Cat# MS-102-3001). Sequencing reads were trimmed using fastp v0.21.0 (Chen et al., 2018) and subsequently mapped to the viral genome sequences of a lineage A isolate (strain WK-521; GISAID ID: EPI_ISL_408667) (Matsuyama et al., 2020) using BWA-MEM v0.7.17 (Li and Durbin, 2009). Variant calling, filtering, and annotation were performed using SAMtools v1.9 (Li et al., 2009) and snpEff v5.0e (Cingolani et al., 2012).

Phylogenetic and comparative genome analyses

To construct a maximum likelihood tree of Omicron lineages (BA.1, BA.1.1, BA.2, and BA.3) sampled from South Africa, the genome sequence data of SARS-CoV-2 and its metadata were downloaded from the GISAID database (https://www.gisaid.org/) (Khare et al., 2021) on January 26, 2022. We excluded the data of viral strains with the following features from the analysis: i) a lack collection date information; ii) sampling from animals other than humans; iii) a low-coverage sequencing flag; or iv) >2% undetermined nucleotide characters. All the BA.2 and BA.3 sequences and 200 randomly sampled BA.1 (including 20 BA.1.1) sequences were used for tree construction, in addition to an outgroup sequence, EPI_ISL_466615, representing the oldest isolate of B.1.1 obtained in the UK. The viral genome sequences were mapped to the reference sequence of Wuhan-Hu-1 (GenBank accession no.: NC_045512.2) using Minimap2 v2.17 (Li, 2018) and subsequently converted to a multiple sequence alignment according to the GISAID phylogenetic analysis pipeline (https://github.com/roblanf/sarscov2phylo). The alignment sites corresponding to the 1–265 and 29674–29903 positions in the reference genome were masked (i.e., converted to NNN). Alignment sites at which >50% of sequences contained a gap or undetermined/ambiguous nucleotide were trimmed using trimAl v1.2 (Capella-Gutiérrez et al., 2009). Phylogenetic tree construction was performed via a three-step protocol: i) the first tree was constructed; ii) tips with longer external branches (Z score > 4) were removed from the dataset; iii) and the final tree was constructed. Tree reconstruction was performed by RAxML v8.2.12 (Stamatakis, 2014) under the GTRCAT substitution model. The node support value was calculated by 100 times bootstrap analysis.

We performed the phylodynamic analysis of Omicron lineages (BA.1, BA.1.1, BA.2 and BA.3) sampled from South Africa as described below. The SARS-CoV-2 genome sequence dataset used above was split into each Omicron lineage. As an outgroup, the oldest BA.2 sequence (GISAID ID: EPI_ISL_8128463) was added to the BA.1 and BA.3 datasets, and the oldest BA.3 sequence (GISAID ID: EPI_ISL_8616600) was added to the BA.2 dataset. The multiple sequence alignment was constructed as described above. A time-calibrated tree of each lineage was constructed by BEAST2 v2.6.6 (Bouckaert et al., 2014). The HKY model (Hasegawa et al., 1985) with four categories of discrete gamma rate variation was selected as a nucleotide substitution model. A relaxed molecular clock modelled based on a log-normal distribution was selected. The exponential growth coalescent model was used. For the BA.1, BA.2, and BA.3 datasets, nineteen, four, and three independent Markov chain Monte Carlo (MCMC) chains were run with 2,000,000 warmup and 18,000,000 sampling iterations, respectively. We confirmed that the effective sampling sizes for all parameters were greater than 200, indicating that the MCMC runs were successfully convergent. The maximum credible trees with common ancestor heights are shown in Figure S1.

The numbers of amino acid differences (including nonsynonymous substitutions, insertions, and deletions) between SARS-CoV-2 lineages were identified as follows (see "Modeling the epidemic dynamics of SARS-CoV-2 lineages" section). Information on the amino acid differences of each viral strain compared with the reference sequence of Wuhan-Hu-1 (GenBank accession no.: NC_045512.2) was extracted from GISAID metadata (downloaded on January 26, 2022). In each viral lineage, the amino acid differences that were present in >10% sequences were extracted and subsequently counted. For the comparison of BA.1 and BA.2, the set of symmetric amino acid differences compared with the reference was determined, and the number of differences was subsequently counted.

Modeling the epidemic dynamics of SARS-CoV-2 lineages

To quantify the spread rate of each SARS-CoV-2 lineage in the human population, we estimated the relative effective reproduction number of each viral lineage according to the epidemic dynamics, calculated on the basis of viral genomic surveillance data. The data

were downloaded from the GISAID database (https://www.gisaid.org/) on February 1, 2022. We excluded the data of viral strains with the following features from the analysis: i) a lack of collection date information; ii) sampling in animals other than humans; or iii) sampling by quarantine. We analyzed the datasets of the eleven countries with >100 available BA.2 sequences (Austria, Denmark, Germany, India, Israel, the Philippines, Singapore, South Africa, Sweden, the UK, and the USA) (Figures 1 and S2). The dynamics of BA.1, BA.1.1, BA.2, and Delta (B.1.617.2 and AY lineages) in each country from October 1, 2021, to January 25, 2022, were analyzed. The number of viral sequences of each viral lineage collected on each day in each country was counted. Finally, we constructed an L (lineage) × C (country) × T (time) = 4 × 11 × 117-shaped array, which comprises the count of each viral lineage in each country on each day. This array was used as input data for the statistical model described below.

We constructed a Bayesian hierarchical model to represent relative lineage growth dynamics with multinomial logistic regression. The mathematical theory underlying the model is described in detail elsewhere (Obermeyer et al., 2022; Vöhringer et al., 2021), and this model was similar to the model used in our previous study (Suzuki et al., 2022). In the present study, we incorporated a hierarchical structure into the slope parameter over time, which enabled us to estimate the global average relative effective reproduction number of each viral lineage as well as the value for each country. Arrays in the model index over one or more indices: L = 4 viral lineages l; C = 11 countries c; and T = 117 days t. The model is:

$$\beta_{lc} \sim \text{Student\_t}(6, \beta_l, \sigma_l)$$

$$\mu_{lct} = \alpha_{lc} + \beta_{lc} t$$

$$\theta_{.ct} = \text{softmax}(\mu_{.ct})$$

$$y_{lct} \sim \text{Multinomial}\left(\sum_l y_{lct}, \theta_{.ct}\right)$$

The explanatory variable was time, t, and the outcome variable was y_{lct}, which represented the count of viral lineage l in country c at time t. The slope parameter of lineage l in country c, β_{lc}, was generated from a Student's t distribution with hyperparameters of the mean, β_l, and the standard deviation, σ_l. As the distribution generating β_{lc}, we used a Student's t distribution with six degrees of freedom instead of a normal distribution to reduce the effects of outlier values of β_{lc}. In the model, the linear estimator $\mu_{.ct}$, consisting of the intercept $\alpha_{.c}$ and the slope $\beta_{.c}$, was converted to the simplex $\theta_{.ct}$, which represented the probability of occurrence of each viral lineage at time t in country c, based on the softmax link function defined as:

$$\text{softmax}(x) = \frac{\exp(x)}{\sum_i \exp(x_i)}$$

y_{lct} is generated from $\theta_{.ct}$ and the total count of all lineages at time t in country c according to a multinomial distribution.

The relative effective reproduction number of each viral lineage in each county (r_{lc}) was calculated according to the slope parameter β_{lc} as:

$$r_{lc} = \exp(\gamma \beta_{lc})$$

where γ is the average viral generation time (2.1 days) (http://sonorouschocolate.com/covid19/index.php?title=Estimating_Generation_Time_Of_Omicron). Similarly, the global average relative effective reproduction number of each viral lineage was calculated according to the slope hyperparameter β_l as:

$$r_l = \exp(\gamma \beta_l)$$

For parameter estimation, the intercept and slope parameters of the BA.1 variant were fixed at 0. Consequently, the relative effective reproduction number of BA.1 was fixed at 1, and those of the other lineages were estimated relative to that of BA.1.

Parameter estimation was performed via the MCMC approach implemented in CmdStan v2.28.1 (https://mc-stan.org) with CmdStanr v0.4.0 (https://mc-stan.org/cmdstanr/). Noninformative priors were set for all parameters. Four independent MCMC chains were run with 1,000 and 2,000 steps in the warmup and sampling iterations, respectively. We confirmed that all estimated parameters showed <1.01 R-hat convergence diagnostic values and >200 effective sampling size values, indicating that the MCMC runs were successfully convergent. The fitted model closely recapitulated the observed viral lineage dynamics in each country (Figure S2C). The above analyses were performed in R v4.1.2 (https://www.r-project.org/). Information on the relative effective reproduction number of BA.2 estimated in the present study is summarized in Table S1.

To validate our statistical model used in the present study, we compared the effective reproduction number of BA.2 relative to that of BA.1 in Denmark estimated by our model and that by another group (Ito et al., 2022). We confirmed that the relative effective

reproduction number of BA.2 in Denmark estimated by our model (1.28) is comparative with that by the previous study (1.26) (Table S1).

Plasmid construction

Plasmids expressing the SARS-CoV-2 S proteins of B.1.1 (the parental D614G-bearing variant), Alpha (B.1.1.7), Delta (B.1.617.2) and BA.1 variants were prepared in our previous studies (Kimura et al., 2022; Meng et al., 2022; Motozono et al., 2021; Ozono et al., 2021; Saito et al., 2022; Suzuki et al., 2022). Plasmids expressing the codon-optimized S proteins of BA.2 and a BA.2 derivative that loses its cytoplasmic tail were generated by site-directed overlap extension PCR using the primers listed in Table S3. The resulting PCR fragment was digested with KpnI and NotI and inserted into the corresponding site of the pCAGGS vector (Niwa et al., 1991). To construct the plasmids expressing anti-SARS-CoV-2 monoclonal antibodies (casirivimab, imdevimab or sotrovimab), the sequences of the variable regions of these antibodies were obtained from KEGG Drug Database (https://www.genome.jp/kegg/drug/) and were artificially synthesized (Fasmac). The obtained coding sequences of the variable regions of the heavy and light chains were cloned into the pCAGGS vector containing the sequences of the human immunoglobulin 1 and kappa constant region [kindly provided by Dr. Hisashi Arase (Osaka University, Japan)]. Nucleotide sequences were determined by DNA sequencing services (Eurofins), and the sequence data were analyzed by Sequencher v5.1 software (Gene Codes Corporation).

Preparation of monoclonal antibodies

Casirivimab, imdevimab and sotrovimab were prepared as previously described (Liu et al., 2021b; Meng et al., 2022). Briefly, the pCAGGS vectors containing the sequences encoding the immunoglobulin heavy and light chains were cotransfected into HEK293T cells using PEI Max (Polysciences, Cat# 24765-1). At 48 h posttransfection, the cell culture supernatants were harvested, and the antibodies were purified using NAb protein A plus spin kit (Thermo Fisher Scientific, Cat# 89948) according to the manufacturer's protocol.

Preparation of mouse sera

The SARS-CoV-2 S-immunized mouse sera were prepared as previously described (Liu et al., 2021b). To prepare the immunogen, B16F10 cells (2,500,000 cells) were transfected with 5 μg S expression plasmid by PEI Max (Polysciences, Cat# 24765-1) according to the manufacturer's protocol. Two days posttransfection, the transfected cells were washed twice with PBS, and then the cell pellets were stored at –80°C (10,000,000 cells per stock). The expression of transfected S protein was verified by flow cytometry and western blot. BALB/c mice (female, 7 weeks old) were purchased from Japan SLC Inc. (Shizuoka, Japan). The mice were maintained under specific pathogen-free conditions. For the immunization, mice were subcutaneously immunized with the freeze-thawed S-expressing B16F10 cells in 50% complete Freund's adjuvant (Sigma-Aldrich, Cat# F5881). Three weeks after immunization, blood was collected in BD microtainer blood collection tubes (BD Biosciences, Cat# 365967) and sera were collected by centrifugation.

Neutralization assay

Pseudoviruses were prepared as previously described (Kimura et al., 2022; Meng et al., 2022; Ozono et al., 2021; Saito et al., 2022; Uriu et al., 2021). Briefly, lentivirus (HIV-1)-based, luciferase-expressing reporter viruses were pseudotyped with the SARS-CoV-2 spikes. HEK293T cells (1,000,000 cells) were cotransfected with 1 μg psPAX2-IN/HiBiT (Ozono et al., 2020), 1 μg pWPI-Luc2 (Ozono et al., 2020), and 500-ng plasmids expressing parental S or its derivatives using PEI Max (Polysciences, Cat# 24765-1) according to the manufacturer's protocol. Two days posttransfection, the culture supernatants were harvested and centrifuged. The pseudoviruses were stored at –80°C until use.

Neutralization assay was prepared as previously described (Kimura et al., 2022; Meng et al., 2022; Ozono et al., 2021; Saito et al., 2022; Uriu et al., 2021). Briefly, the SARS-CoV-2 S pseudoviruses (counting ~20,000 relative light units) were incubated with serially diluted (40-fold to 29,160-fold dilution at the final concentration) heat-inactivated sera or monoclonal antibodies (casirivimab, imdevimab or sotrovimab) at 37°C for 1 h. Pseudoviruses without sera were included as controls. Then, an 80 μl mixture of pseudovirus and serum/antibody was added to HOS-ACE2/TMPRSS2 cells (10,000 cells/50 μl) in a 96-well white plate. At 2 d.p.i., the infected cells were lysed with a One-Glo luciferase assay system (Promega, Cat# E6130) or a Bright-Glo™ Luciferase Assay System (Promega, Cat# E2650), and the luminescent signal was measured using a GloMax explorer multimode microplate reader 3500 (Promega) or CentroXS3 (Berthhold Technologies). The assay of each serum was performed in triplicate, and the 50% neutralization titer (NT50) was calculated using Prism 9 software v9.1.1 (GraphPad Software).

SARS-CoV-2 reverse genetics

Recombinant SARS-CoV-2 was generated by circular polymerase extension reaction (CPER) as previously described (Motozono et al., 2021; Saito et al., 2022; Torii et al., 2021). In brief, 9 DNA fragments encoding the partial genome of SARS-CoV-2 (strain WK-521, PANGO lineage A; GISAID ID: EPI_ISL_408667) (Matsuyama et al., 2020) were prepared by PCR using PrimeSTAR GXL DNA polymerase (Takara, Cat# R050A). A linker fragment encoding hepatitis delta virus ribozyme, bovine growth hormone poly A signal and cytomegalovirus promoter was also prepared by PCR. The corresponding SARS-CoV-2 genomic region and the PCR templates and primers used for this procedure are summarized in Table S3. The 10 obtained DNA fragments were mixed and used for CPER (Torii et al., 2021). To prepare GFP-expressing replication-competent recombinant SARS-CoV-2, we used fragment 9, in which

the *GFP* gene was inserted in the *ORF7a* frame, instead of the authentic F9 fragment (see Figure 3A and Table S3) (Torii et al., 2021).

To generate chimeric recombinant SARS-CoV-2, rBA.1 S-GFP and rBA.2 S-GFP (summarized in Figure 3A), mutations were inserted in fragment 8 (Table S3) using the GENEART site-directed mutagenesis system (Thermo Fisher Scientific, Cat# A13312) according to the manufacturer's protocol with the primers listed in Table S3. A recombinant SARS-CoV-2 that bears D614G S (rB.1.1 S-GFP) was prepared in our previous study (Saito et al., 2022). To prepare a rDelta S-GFP (Figure 3A), the fragment of viral genome that corresponds to the region of fragment 8 (Table S3) was subcloned from a Delta isolate (strain TKYTK1734; GISAID ID: EPI_ISL_2378732) (Saito et al., 2022). Nucleotide sequences were determined by a DNA sequencing service (Fasmac), and the sequence data were analyzed by Sequencher software v5.1 (Gene Codes Corporation).

To produce recombinant SARS-CoV-2 (seed viruses), the CPER products were transfected into HEK293-C34 cells using TransIT-LT1 (Takara, Cat# MIR2300) according to the manufacturer's protocol. At one day posttransfection, the culture medium was replaced with DMEM (high glucose) (Sigma-Aldrich, Cat# 6429-500ML) containing 2% FBS, 1% PS and doxycycline (1 μg/ml; Takara, Cat# 1311N). At six days posttransfection, the culture medium was harvested and centrifuged, and the supernatants were collected as the seed virus. To remove the CPER products (i.e., SARS-CoV-2-related DNA), 1 ml of the seed virus was treated with 2 μl TURBO DNase (Thermo Fisher Scientific, Cat# AM2238) and incubated at 37°C for 1 hr. Complete removal of the CPER products from the seed virus was verified by PCR. The working virus stock was prepared using the seed virus as described below (see "SARS-CoV-2 preparation and titration" section).

SARS-CoV-2 preparation and titration

The working virus stocks of chimeric recombinant SARS-CoV-2 (rB.1.1 S-GFP, rDelta S-GFP, rBA.1 S-GFP and rBA.2 S-GFP) were prepared and titrated as previously described (Motozono et al., 2021; Saito et al., 2022; Torii et al., 2021). In brief, 20 μl of the seed virus was inoculated into VeroE6/TMPRSS2 cells (5,000,000 cells in a T-75 flask). One hour postinfection (h.p.i.), the culture medium was replaced with DMEM (low glucose) (Wako, Cat# 041-29775) containing 2% FBS and 1% PS. At 3 d.p.i., the culture medium was harvested and centrifuged, and the supernatants were collected as the working virus stock.

The titer of the prepared working virus was measured as the 50% tissue culture infectious dose ($TCID_{50}$). Briefly, one day before infection, VeroE6/TMPRSS2 cells (10,000 cells) were seeded into a 96-well plate. Serially diluted virus stocks were inoculated into the cells and incubated at 37°C for 4 d. The cells were observed under microscopy to judge the CPE appearance. The value of $TCID_{50}$/ml was calculated with the Reed–Muench method (Reed and Muench, 1938).

To verify the sequence of chimeric recombinant SARS-CoV-2, viral RNA was extracted from the working viruses using a QIAamp viral RNA mini kit (Qiagen, Cat# 52906) and viral genome sequence was analyzed as described above (see "Viral genome sequencing" section). In brief, the viral sequences of rB.1.1 S-GFP, rDelta S-GFP, rBA.1 S-GFP and rBA.2 S-GFP were used for the reference. Information on the unexpected mutations detected is summarized in Table S4, and the raw data are deposited in Gene Expression Omnibus (accession number: GSE196649).

SARS-CoV-2 infection

One day before infection, Vero cells (10,000 cells), VeroE6/TMPRSS2 cells (10,000 cells), Calu-3 cells (20,000 cells), HEK293-ACE2 cells (10,000 cells), HEK293-ACE2/TMPRSS2 cells (10,000 cells), were seeded into a 96-well plate. SARS-CoV-2 [100 $TCID_{50}$ for VeroE6/TMPRSS2 cells (Figure 3B), 1,000 $TCID_{50}$ for Vero cells (Figure 3B), HEK293-ACE2 cells (10,000 cells) (Figure 3N), and HEK293-ACE2/TMPRSS2 cells (10,000 cells) (Figure 3N); and 2,000 $TCID_{50}$ for Calu-3 cells (Figure 3B)] was inoculated and incubated at 37°C for 1 hr. The infected cells were washed, and 180 μl culture medium was added. The culture supernatant (10 μl) was harvested at the indicated timepoints and used for RT–qPCR to quantify the viral RNA copy number (see "RT–qPCR" section below).

The infection experiment primary human nasal epithelial cells (Figure 3B) was performed as previously described (Meng et al., 2022; Saito et al., 2022). Briefly, the working viruses were diluted with Opti-MEM (Thermo Fisher Scientific, Cat# 11058021). The diluted viruses (1,000 $TCID_{50}$ in 100 μl) were inoculated onto the apical side of the culture and incubated at 37°C for 1 h. The inoculated viruses were removed and washed twice with Opti-MEM. To harvest the viruses on the apical side of the culture, 100 μl Opti-MEM was applied onto the apical side of the culture and incubated at 37°C for 10 m. The Opti-MEM applied was harvested and used for RT–qPCR to quantify the viral RNA copy number (see "RT–qPCR" section below).

RT–qPCR

RT–qPCR was performed as previously described (Meng et al., 2022; Motozono et al., 2021; Saito et al., 2022; Suzuki et al., 2022). Briefly, 5 μl culture supernatant was mixed with 5 μl 2 × RNA lysis buffer [2% Triton X-100 (Nacalai Tesque, Cat# 35501-15), 50 mM KCl, 100 mM Tris-HCl (pH 7.4), 40% glycerol, 0.8 U/μl recombinant RNase inhibitor (Takara, Cat# 2313B)] and incubated at room temperature for 10 m. RNase-free water (90 μl) was added, and the diluted sample (2.5 μl) was used as the template for real-time RT-PCR performed according to the manufacturer's protocol using One Step TB Green PrimeScript PLUS RT-PCR kit (Takara, Cat# RR096A) and the following primers: Forward *N*, 5'-AGC CTC TTC TCG TTC CTC ATC AC-3'; and Reverse *N*, 5'-CCG CCA TTG CCA GCC ATT C-3'. The viral RNA copy number was standardized with a SARS-CoV-2 direct detection RT-qPCR kit (Takara,

Cat# RC300A). Fluorescent signals were acquired using QuantStudio 3 Real-Time PCR system (Thermo Fisher Scientific), CFX Connect Real-Time PCR Detection system (Bio-Rad), Eco Real-Time PCR System (Illumina), qTOWER3 G Real-Time System (Analytik Jena) or 7500 Real-Time PCR System (Thermo Fisher Scientific).

Fluorescence microscopy

Fluorescence microscopy (Figures 3C and S3A) was performed as previously described (Saito et al., 2022; Suzuki et al., 2022). Briefly, one day before infection, VeroE6/TMPRSS2 cells (10,000 cells) were seeded into 96-well, glass bottom, black plates and infected with SARS-CoV-2 (100 $TCID_{50}$). At 24, 48, and 72 h.p.i., GFP fluorescence was observed under an All-in-One Fluorescence Microscope BZ-X800 (Keyence) in living cells, and a 13-square-millimeter-mm^2 area of each sample was scanned. Images were reconstructed using an BZ-X800 analyzer software (Keyence), and the area of the GFP-positive cells was measured using this software.

Plaque assay

Plaque assay (Figure 3D) was performed as previously described (Motozono et al., 2021; Saito et al., 2022; Suzuki et al., 2022). Briefly, one day before infection, VeroE6/TMPRSS2 cells (100,000 cells) were seeded into a 24-well plate and infected with SARS-CoV-2 (1, 10, 100 and 1,000 $TCID_{50}$) at 37°C for 2 h. Mounting solution containing 3% FBS and 1.5% carboxymethyl cellulose (Wako, Cat# 039-01335) was overlaid, followed by incubation at 37°C. At 3 d.p.i., the culture medium was removed, and the cells were washed with PBS three times and fixed with 4% paraformaldehyde phosphate (Nacalai Tesque, Cat# 09154-85). The fixed cells were washed with tap water, dried, and stained with staining solution [0.1% methylene blue (Nacalai Tesque, Cat# 22412-14) in water] for 30 m. The stained cells were washed with tap water and dried, and the size of plaques was measured using Fiji software v2.2.0 (ImageJ).

Coculture experiment

Coculture experiment (Figure S3B) was performed as previously described (Suzuki et al., 2022). This assay utilizes a dual split protein (DSP) encoding *Renilla* luciferase and *GFP* genes; the respective split proteins, DSP_{8-11} and DSP_{1-7}, are expressed in effector and target cells by transfection. Briefly, one day before transfection, effector cells (i.e., S-expressing cells) were seeded on the poly-L-lysine (Sigma, Cat# P4832) coated coverslips put in a 12-well plate, and target cells were prepared at a density of 100,000 cells in a 12-well plate. To prepare effector cells, HEK293 cells were cotransfected with the S-expression plasmids (500 ng) and $pDSP_{8-11}$ (500 ng) using PEI Max (Polysciences, Cat# 24765-1). To prepare target cells, HEK293 and HEK293-ACE2/TMPRSS2 cells were transfected with $pDSP_{1-7}$ (500 ng) (Kondo et al., 2011). At 24 hr posttransfection, target cells were detached and cocultured with effector cells in a 1:2 ratio. At 9 h post-coculture, cells were fixed with 4% paraformaldehyde in PBS (Nacalai Tesque, Cat# 09154-85) for 15 m at room temperature. Nuclei were stained with Hoechst 33342 (Thermo Fisher Scientific, Cat# H3570). The coverslips were mounted on glass slides using Fluoromount-G (Southern Biotech, Cat# 0100-01) with Hoechst 33342 and observed using an A1Rsi Confocal Microscope (Nikon). The size of syncytium (GFP-positive area) was measured using Fiji software v2.2.0 (ImageJ) as previously described (Suzuki et al., 2022).

SARS-CoV-2 S-based fusion assay

SARS-CoV-2 S-based fusion assay (Figures 3F and 3K) was performed as previously described (Motozono et al., 2021; Saito et al., 2022; Suzuki et al., 2022). Briefly, on day 1, effector cells (i.e., S-expressing cells) and target cells (see below) were prepared at a density of 0.6–0.8 × 10^6 cells in a 6-well plate. To prepare effector cells, HEK293 cells were cotransfected with the S expression plasmids (400 ng) and $pDSP_{8-11}$ (Kondo et al., 2011) (400 ng) using TransIT-LT1 (Takara, Cat# MIR2300). To prepare target cells, HEK293 cells were cotransfected with pC-ACE2 (Ozono et al., 2021) (200 ng) and $pDSP_{1-7}$ (Kondo et al., 2011) (400 ng). Target HEK293 cells in selected wells were cotransfected with pC-TMPRSS2 (Ozono et al., 2021) (40 ng) in addition to the plasmids above. VeroE6/TMPRSS2 cells, HEK293-ACE2 cells and HEK293-ACE2/TMPRSS2 cells were transfected with $pDSP_{1-7}$ (400ng). On day 3 (24 h posttransfection), 16,000 effector cells were detached and reseeded into 96-well black plates (PerkinElmer, Cat# 6005225), and target cells (HEK293 cells, VeroE6/TMPRSS2 or Calu-3/DSP_{1-7} cells) were reseeded at a density of 1,000,000 cells/2 ml/well in 6-well plates. On day 4 (48 h posttransfection), target cells were incubated with EnduRen live cell substrate (Promega, Cat# E6481) for 3 h and then detached, and 32,000 target cells were added to a 96-well plate with effector cells. *Renilla* luciferase activity was measured at the indicated time points using Centro XS3 LB960 (Berthhold Technologies). To measure the surface expression level of S protein, effector cells were stained with rabbit anti-SARS-CoV-2 S S1/S2 polyclonal antibody (Thermo Fisher Scientific, Cat# PA5-112048, 1:100). Normal rabbit IgG (Southern Biotech, Cat# 0111-01, 1:100) was used as negative controls, and APC-conjugated goat anti-rabbit IgG polyclonal antibody (Jackson ImmunoResearch, Cat# 111-136-144, 1:50) was used as a secondary antibody. Surface expression level of S proteins (Figure 3E) was measured using FACS Canto II (BD Biosciences) and the data were analyzed using FlowJo software v10.7.1 (BD Biosciences). To calculate fusion activity, *Renilla* luciferase activity was normalized to the MFI of surface S proteins. The normalized value (i.e., *Renilla* luciferase activity per the surface S MFI) is shown as fusion activity.

Western blot

Western blot (Figure 3G) was performed as previously described (Motozono et al., 2021; Saito et al., 2022; Suzuki et al., 2022). The HEK293 cells cotransfected with the S expression plasmids and the plasmids for pseudovirus production (see "Neutralization assay"

section above) were used. To quantify the level of the cleaved S2 protein in the cells, the harvested cells were washed and lysed in lysis buffer [25 mM HEPES (pH 7.2), 20% glycerol, 125 mM NaCl, 1% Nonidet P40 substitute (Nacalai Tesque, Cat# 18558-54), protease inhibitor cocktail (Nacalai Tesque, Cat# 03969-21)]. After quantification of total protein by protein assay dye (Bio-Rad, Cat# 5000006), lysates were diluted with 2 × sample buffer [100 mM Tris-HCl (pH 6.8), 4% SDS, 12% β-mercaptoethanol, 20% glycerol, 0.05% bromophenol blue] and boiled for 10 m. Then, 10 μl samples (50 μg of total protein) were subjected to western blot. To quantify the level of the S2 protein in the virions, the culture supernatant (900 μl) was layered onto 500 μl 20% sucrose in PBS and centrifuged at 20,000 g for 2 h at 4°C. The pelleted virions were resuspended in 1× NuPAGE LDS sample buffer (Thermo Fisher Scientific, Cat# NP0007) containing 2% β-mercaptoethanol and incubated at 70°C for 10 m. For protein detection, the following antibodies were used: mouse anti-SARS-CoV-2 S monoclonal antibody (clone 1A9, GeneTex, Cat# GTX632604, 1:10,000), mouse anti-HIV-1 p24 monoclonal antibody (clone 183-H12-5C, obtained from the Nih HIV Reagent Program, Cat# ARP-3537, 1:2,000), rabbit anti-beta actin (ACTB) monoclonal antibody (clone 13E5, Cell Signaling, Cat# 4970, 1:5,000), horseradish peroxidase (HRP)-conjugated donkey anti-rabbit IgG polyclonal antibody (Jackson ImmunoResearch, Cat# 711-035-152, 1:10,000) and HRP-conjugated donkey anti-mouse IgG polyclonal antibody (Jackson ImmunoResearch, Cat# 715-035-150, 1:10,000). Chemiluminescence was detected using SuperSignal west femto maximum sensitivity substrate (Thermo Fisher Scientific, Cat# 34095) according to the manufacturer's instruction. Bands were visualized using an Amersham Imager 600 (GE Healthcare), and the band intensity was quantified using Image Studio Lite v5.2 (LI-COR Biosciences) or Fiji software v2.2.0 (ImageJ).

Pseudovirus infection

Pseudovirus infection was (Figures 3H and 3L) performed as previously described (Kimura et al., 2022; Meng et al., 2022; Motozono et al., 2021; Saito et al., 2022; Suzuki et al., 2022; Uriu et al., 2021). Briefly, the amount of pseudoviruses prepared was quantified by the HiBiT assay using Nano Glo HiBiT lytic detection system (Promega,Cat# N3040) as previously described (Ozono et al., 2021; Ozono et al., 2020), and the same amount of pseudoviruses (normalized to the HiBiT value, which indicates the amount of p24 HIV-1 antigen) was inoculated into HOS-ACE2/TMPRSS2 cells, HEK293-ACE2 cells or HEK293-ACE2/TMPRSS2 and viral infectivity was measured as described above (see "Neutralization assay" section). To analyze the effect of TMPRSS2 for pseudovirus infectivity (Figure 3L), the fold change of the values of HEK293-ACE2/TMPRSS2 to HEK293-ACE2 was calculated.

Yeast surface display

Yeast surface display (Figure 3I) was performed as previously described as previously described (Dejnirattisai et al., 2022; Kimura et al., 2022; Motozono et al., 2021; Zahradník et al., 2021a). Briefly, the peptidase domain of human ACE2 (residues 18-740) was expressed in Expi293F cells and purified by a 5-ml HisTrap Fast Flow column (Cytiva, Cat# 17-5255-01) and Superdex 200 16/600 (Cytiva, Cat# 28-9893-35) using an ÄKTA pure chromatography system (Cytiva), and the purified soluble ACE2 was labelled with CF640 (Biotium, Cat# 92108). Protein quality was verified using a Tycho NT.6 system (NanoTemper) and ACE2 activity assay kit (SensoLyte, Cat# AS-72086).

An enhanced yeast display platform for SARS-CoV-2 RBD [wild-type (B.1.1), residues 336-528] yeast surface expression was established using *Saccharomyces cerevisiae* strain EBY100 (ATCC, MYA-4941) and pJYDC1 plasmid (Addgene, Cat# 162458) as previously described (Dejnirattisai et al., 2022; Kimura et al., 2022; Motozono et al., 2021; Zahradník et al., 2021b). The yeast-optimized SARS-CoV-2_RBD-Omicron-BA.1 gene (Dejnirattisai et al., 2022) was obtained from Twist Biosciences. The site-directed mutagenesis was performed using the KAPA HiFi HotStart ReadyMix kit (Roche, Cat# KK2601) and primers listed in Table S3 by restriction enzyme-free cloning procedure (Peleg and Unger, 2014).

The binding affinity of SARS-CoV-2 S B.1.1, BA.1, and BA.2 RBDs to human ACE2 were titrated by flow cytometry. The CF640-labelled ACE2 at 12–14 different concentrations (200 nM to 13 pM in PBS supplemented with bovine serum albumin at 1 g/l) per measurement were incubated with expressed yeast aliquots and 1 nM bilirubin (Sigma-Aldrich, Cat# 14370-1G) and analyzed by using FACS S3e cell sorter device (Bio-Rad) as previously described (Kimura et al., 2022; Motozono et al., 2021; Zahradník et al., 2021b). The background binding subtracted fluorescent signal was fitted to a standard noncooperative Hill equation by nonlinear least-squares regression using Python v3.7 (https://www.python.org) as previously described (Zahradník et al., 2021b).

TMPRSS2 expression on the cell surface

To measure the surface expression level of TMPRSS2 (Figure 3J), HEK293-ACE2 cells and HEK293-ACE2/TMPRSS2 cells were stained with rabbit anti-TMPRSS2 polyclonal antibody (BIOSS, Cat# BS-6285R, 1:100). Normal rabbit IgG (Southern Biotech, Cat# 0111-01, 1:100) was used as negative controls, and APC-conjugated goat anti-rabbit IgG polyclonal antibody (Jackson ImmunoResearch, Cat# 111-136-144, 1:50) was used as a secondary antibody. Surface expression level of TMPRSS2 was measured using FACS Canto II (BD Biosciences) and the data were analyzed using FlowJo software v10.7.1 (BD Biosciences).

E64d treatment

One day before infection, HOS-ACE2-TMPRSS2 cells (10,000 cells) were seeded into a 96-well plate. The next day, the cells were treated with the indicated doses of E64d (Aloxistatin) (Selleck, Cat# S7393) for 1 h, then infected with the pseudoviruses. At 2 d.p.i., the infected cells were lysed with a Bright-Glo luciferase assay system (Promega, Cat# E2620), and the luminescent signal was

measured using a GloMax Explorer Multimode Microplate Reader (Promega). The assay of each pseudovirus was performed in triplicate, and the IC50 was calculated using Prism 9 software v9.1.1 (GraphPad Software).

Cytotoxicity assay

The cytotoxicity of E64d (Aloxistatin) (Figure S3C) was tested using the cell counting kit-8 (Dojindo, Cat# CK04-11) according to the manufacturer's instruction. Briefly, one day before the assay, HOS-ACE2-TMPRSS2 cells (10,000 cells) were seeded into a 96-well plate. The cells were cultured with the serially diluted compound for 48 h. The cell counting kit-8 solution (10 μl) was added to each well, and the cells were incubated at 37°C for 90 m. Absorbance was measured at 450 nm using a GloMax Explorer Microplate Reader (Promega).

Animal experiments

Animal experiments (Figure 4) were performed as previously described (Saito et al., 2022; Suzuki et al., 2022). Syrian hamsters (male, 4 weeks old) were purchased from Japan SLC Inc. (Shizuoka, Japan). Baseline body weights were measured before infection. For the virus infection experiments, hamsters were anaesthetized by intramuscular injection of a mixture of either 0.15 mg/kg medetomidine hydrochloride (Domitor®, Nippon Zenyaku Kogyo), 2.0 mg/kg midazolam (FUJIFILM Wako Chemicals, Cat# 135-13791) and 2.5 mg/kg butorphanol (Vetorphale®, Meiji Seika Pharma), or 0.15 mg/kg medetomidine 0butorphanol. The chimeric recombinant SARS-CoV-2 (rB.1.1 S-GFP, rDelta S-GFP, rBA.1 S-GFP and rBA.2 S-GFP) (10,000 $TCID_{50}$ in 100 μl), or saline (100 μl) were intranasally inoculated under anesthesia. Oral swabs were daily collected under anesthesia with isoflurane (Sumitomo Dainippon Pharma). Body weight, enhanced pause (Penh), the ratio of time to peak expiratory follow relative to the total expiratory time (Rpef) and subcutaneous oxygen saturation (SpO_2) were routinely monitored at indicated timepoints (see "Lung function test" section below). Respiratory organs were anatomically collected at 1, 3 and 5 d.p.i (for lung) or 1 d.p.i. (for trachea). Viral RNA load in the respiratory tissues were determined by RT–qPCR. The respiratory tissues were also used for histopathological and IHC analyses (see "H&E staining" and "IHC" sections below). Sera of infected hamsters were collected at 16 d.p.i. using cardiac puncture under anesthesia with isoflurane and used for neutralization assay (see "Neutralization assay" above).

Lung function test

Lung function test (Figure 4A) was performed as previously described (Suzuki et al., 2022). Respiratory parameters (Penh and Rpef) were measured by using a whole-body plethysmography system (DSI) according to the manufacturer's instructions. In brief, a hamster was placed in an unrestrained plethysmography chamber and allowed to acclimatize for 30 s, then, data were acquired over a 4-m period by using FinePointe Station and Review softwares v2.9.2.12849 (STARR). The state of oxygenation was examined by measuring SpO_2 using pulse oximeter, MouseOx PLUS (STARR). SpO_2 was measured by attaching a measuring chip to the neck of hamsters sedated by 0.25 mg/kg medetomidine hydrochloride.

IHC

IHC (Figures 4C, S2A, and S4B) was performed as previously described (Saito et al., 2022; Suzuki et al., 2022) using an Autostainer Link 48 (Dako). The deparaffinized sections were exposed to EnVision FLEX target retrieval solution high pH (Agilent, Cat# K8004) for 20 m at 97°C to activate, and mouse anti-SARS-CoV-2 N monoclonal antibody (clone 1035111, R&D systems, Cat# MAB10474-SP, 1:400) was used as a primary antibody. The sections were sensitized using EnVision FLEX (Agilent) for 15 m and visualized by peroxidase-based enzymatic reaction with 3,3'-diaminobenzidine tetrahydrochloride (Dako, Cat# DM827) as substrate for 5 m. The N protein positivity (Figures 4D and 4E) was evaluated by certificated pathologists as previously described (Suzuki et al., 2022). Images were incorporated as virtual slide by NDP.scan software v3.2.4 (Hamamatsu Photonics). The N-protein positivity was measured as the area using Fiji software v2.2.0 (ImageJ).

H&E staining

H&E staining (Figures 4F, 4H, and S4C) was performed as previously described (Saito et al., 2022; Suzuki et al., 2022). Briefly, excised animal tissues were fixed with 10% formalin neutral buffer solution, and processed for paraffin embedding. The paraffin blocks were sectioned with 3 μm-thickness and then mounted on MAS-GP-coated glass slides (Matsunami Glass, Cat# Cat# S9901). H&E staining was performed according to a standard protocol.

Histopathological scoring

Histopathological scoring (Figure 4G) was performed as previously described (Saito et al., 2022; Suzuki et al., 2022). Pathological features including bronchitis or bronchiolitis, hemorrhage with congestive edema, alveolar damage with epithelial apoptosis and macrophage infiltration, hyperplasia of type II pneumocytes, and the area of the hyperplasia of large type II pneumocytes were evaluated by certified pathologists and the degree of these pathological findings were arbitrarily scored using four-tiered system as 0 (negative), 1 (weak), 2 (moderate), and 3 (severe). The "large type II pneumocytes" are the hyperplasia of type II pneumocytes exhibiting more than 10-μm-diameter nucleus. We described "large type II pneumocytes" as one of the remarkable histopathological features reacting SARS-CoV-2 infection in our previous studies (Saito et al., 2022; Suzuki et al., 2022). Total histology score is the sum of these five indices.

To measure the inflammation area in the infected lungs (Figure 4I), four hamsters infected with each virus were sacrificed at the 1, 3 and 5 d.p.i., and all four right lung lobes, including upper (anterior/cranial), middle, lower (posterior/caudal), and accessory lobes, were sectioned along with their bronchi. The tissue sections were stained by H&E, and the digital microscopic images were incorporated into virtual slides using NDP.scan software v3.2.4 (Hamamatsu Photonics). The inflammatory area including type II pneumocyte hyperplasia in the infected whole lungs was morphometrically analyzed using Fiji software v2.2.0 (ImageJ).

QUANTIFICATION AND STATISTICAL ANALYSIS

Statistical significance was tested using a two-sided Mann–Whitney *U*-test, a two-sided Student's *t*-test or a two-sided paired *t*-test unless otherwise noted. The tests above were performed using Prism 9 software v9.1.1 (GraphPad Software).

In the time-course experiments (Figures 3B, 3F, 3K, 3N, 4A, 4B, 4D, and 4G), a multiple regression analysis including experimental conditions (i.e., the types of infected viruses) as explanatory variables and timepoints as qualitative control variables was performed to evaluate the difference between experimental conditions thorough all timepoints. *P* value was calculated by a two-sided Wald test. Subsequently, familywise error rates (FWERs) were calculated by the Holm method. These analyses were performed in R v4.1.2 (https://www.r-project.org/).

In Figures 4C, 4F, 4H, and S4, photographs shown are the representative areas of at least two independent experiments by using four hamsters at each timepoint. In Figures 3C and S3, photographs shown are the representatives of >20 fields of view taken for each sample.

CellPress
OPEN ACCESS

Supplemental figures

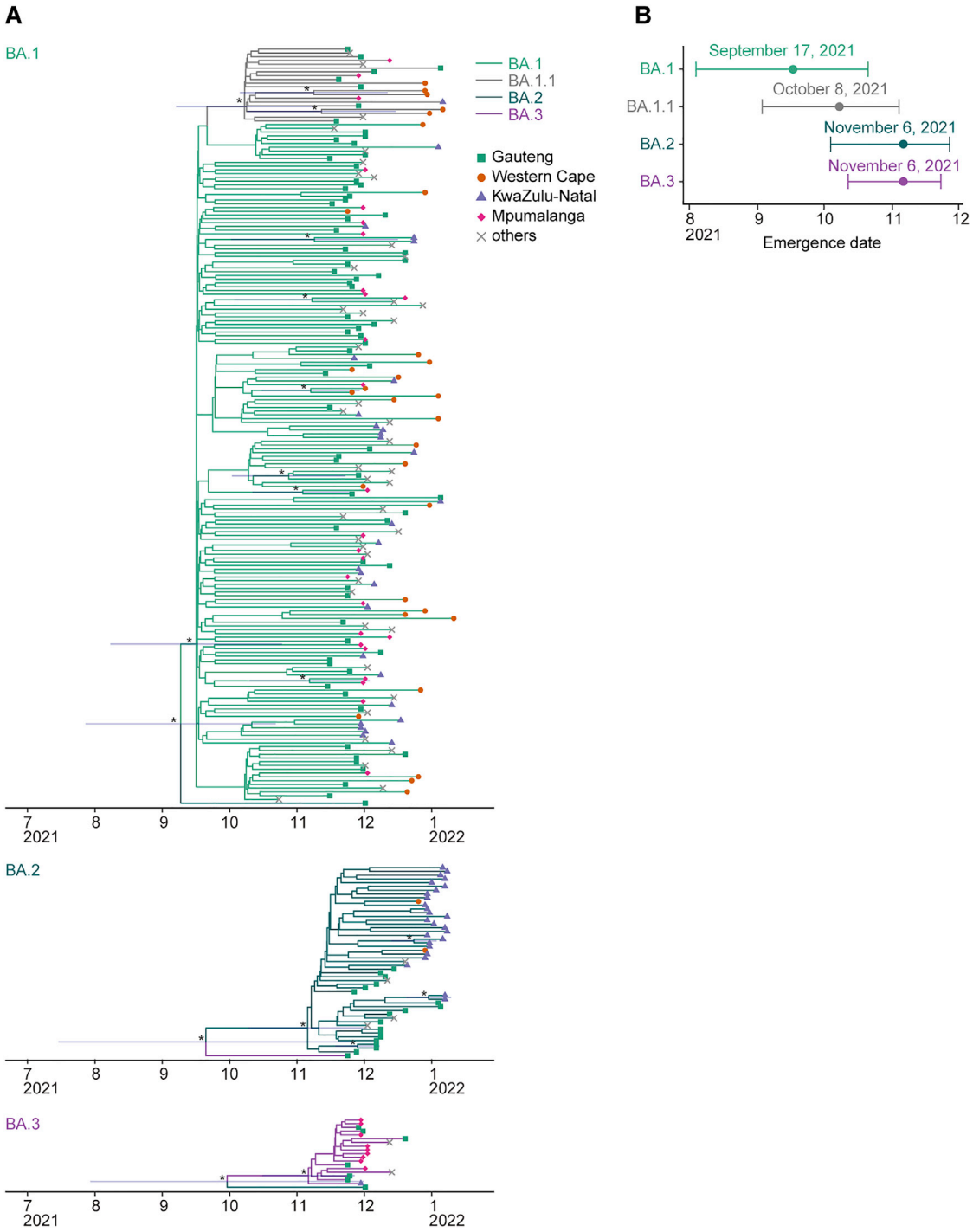

Figure S1. Estimated emergence dates of the Omicron lineages, related to Figure 1

(A) Phylodynamics of BA.1 (top), BA.2 (middle), and BA.3 (bottom) sampled up to January 26, 2022, in South Africa. All BA.2 and BA.3 sequences and 200 randomly sampled BA.1 (including 20 BA.1.1) sequences were used. The time-resolved trees were constructed by using BEAST2. The 95% CI of the divergence time is shown for a node with a $\geq$0.95 posterior value (indicated by an asterisk).

(B) Estimated emergence dates of the Omicron lineages. The 95% CI (error bar) and posterior mean (dot) are shown.

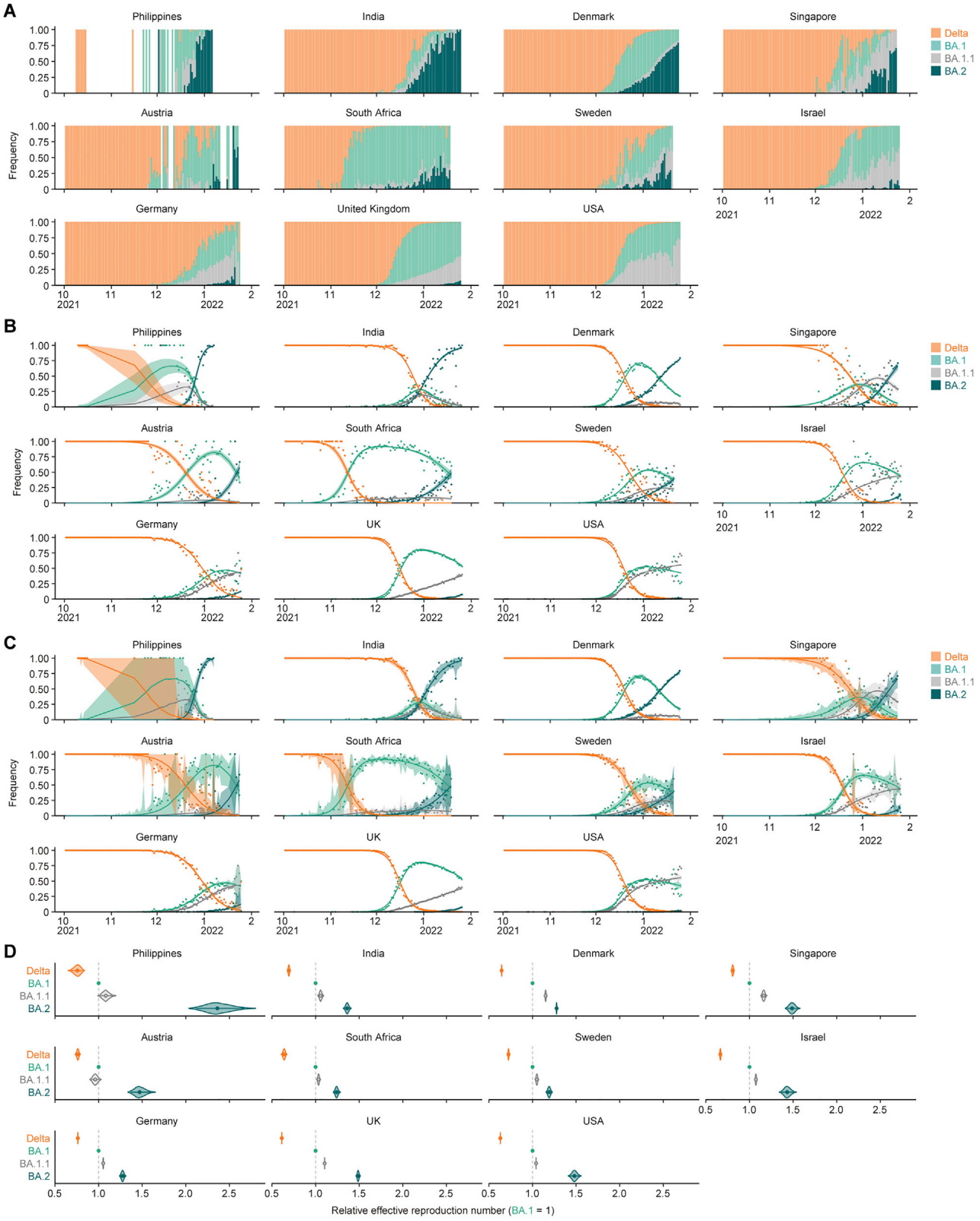

(legend on next page)

Figure S2. Epidemic dynamics of SARS-CoV-2 lineages in countries with a BA.2 epidemic, related to Figure 1

(A) Daily sequence frequency of each viral lineage in eleven countries where ≥100 BA.2 sequences had been reported up to January 25, 2022. These data were used as an input in a Bayesian hierarchical model to estimate epidemic dynamics.

(B and C) Epidemic dynamics of SARS-CoV-2 viral lineages. The observed daily frequency (dot) and the dynamics estimated by the Bayesian model (posterior mean; line) are shown. Additionally, the 95% CI (B) and 90% prediction interval (C) are shown.

(D) Estimated relative effective reproduction number of each viral lineage in each country. The posterior distribution (violin), 95% CI (line), and posterior mean (dot) are shown.

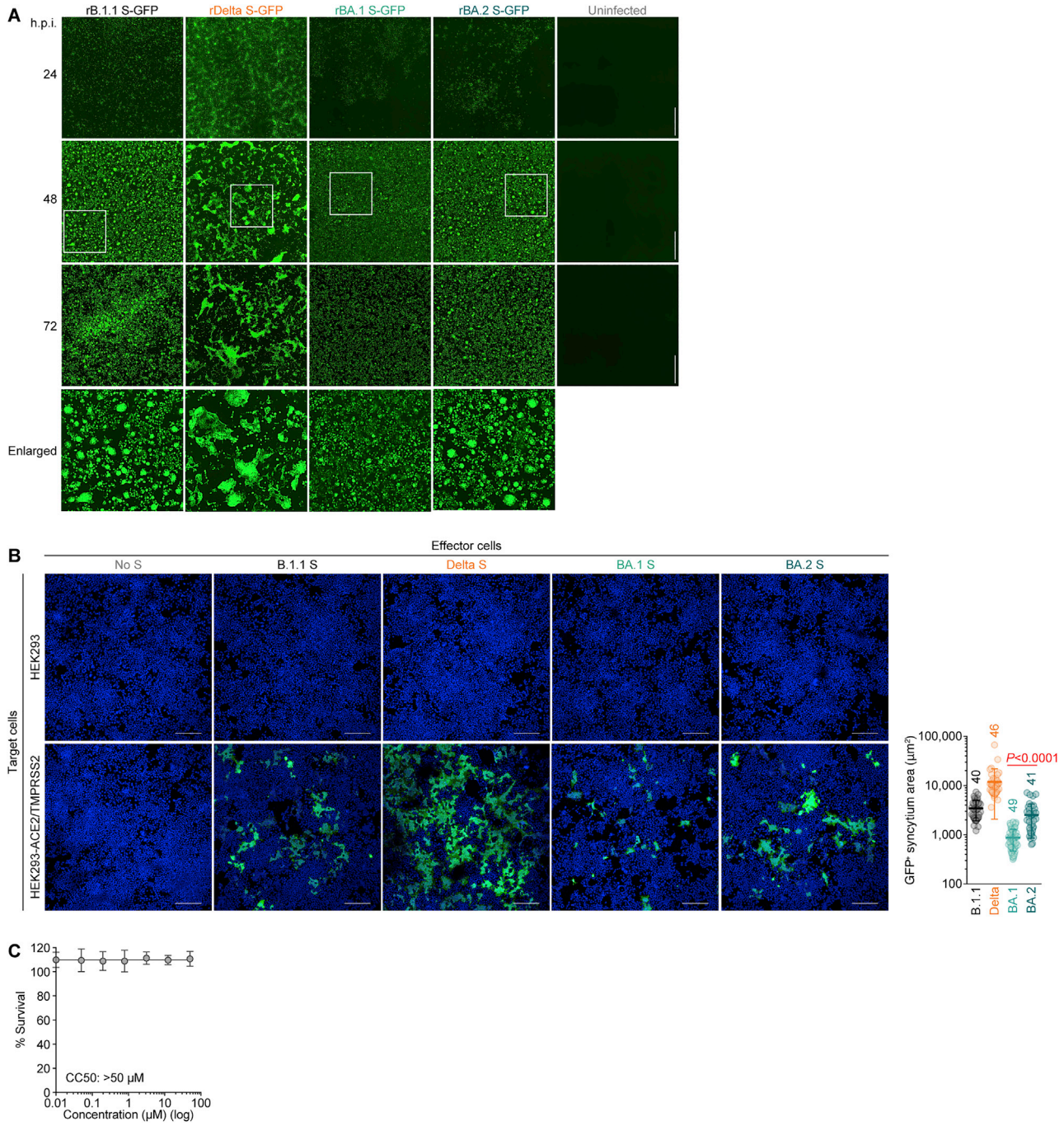

Figure S3. Virological features of BA.2 *in vitro*, related to Figure 3

(A) Fluorescence microscopy. The GFP area were measured in infected VeroE6/TMPRSS2 cells (m.o.i. 0.01) at 24, 48, and 72 h.p.i. Higher-magnification views of the regions indicated by squares are shown at the bottom. The panels at 48 h.p.i. are identical to those shown in Figure 3C.

(B) Coculture of S-expressing cells with HEK293-ACE2/TMPRSS2 cells. Left, representative images of S-expressing cells cocultured with HEK293 cells (top) or HEK293-ACE2/TMPRSS2 cells (bottom). Nuclei were stained with Hoechst 33342 (blue). Right, size distribution of syncytia (green). The numbers in the panel indicate the numbers of GFP-positive syncytia counted.

(C) Cytotoxicity of E64d in HOS-ACE2-TMPRSS2 cells. The cells were cultured in the presence of serially diluted E64d for 48 h, and the cytotoxicity was measured using a cell counting kit-8 solution. The assay for each concentration was performed in sextuplicate, and the data are expressed as the average ± SD. CC50, 50% cytotoxic concentration.

Scale bars, 500 μm (A) or 200 μm (B).

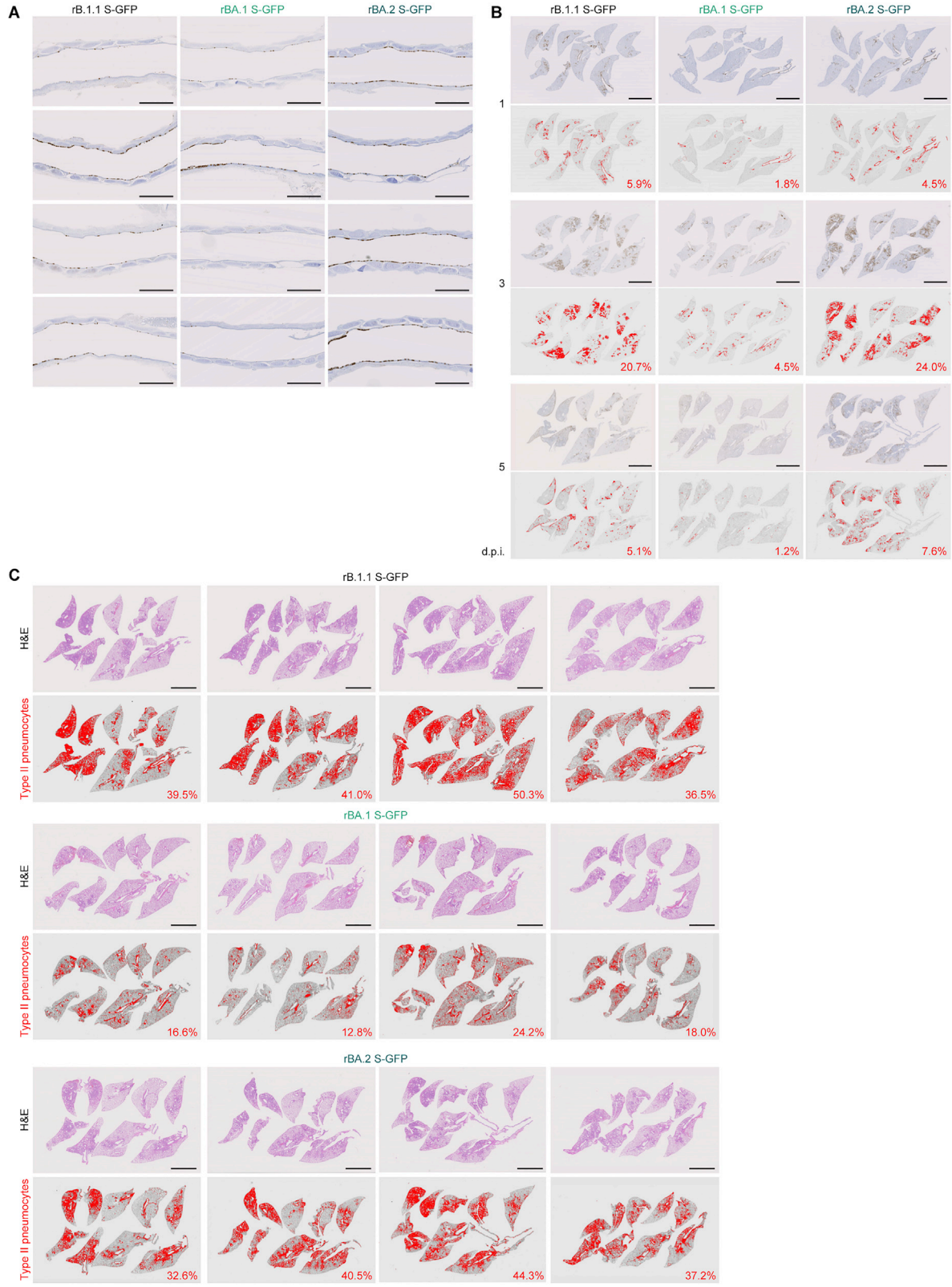

(legend on next page)

Figure S4. Virological features of BA.2 *in vivo*, related to Figure 4

(A) IHC of the viral N protein in the middle portion of the tracheas of all infected hamsters (n = 4 per viral strain) at 1 d.p.i. Each panel shows a representative result from an individual infected hamster.

(B) Right lung lobes of hamsters infected with B.1.1, BA.1 or BA.2 (n = 4 for each virus) at 1, 3 and 5 d.p.i. were immunohistochemically stained with an anti-SARS-CoV-2 N monoclonal antibody. In each panel, IHC staining (top) and the digitalized N-positive area (bottom, indicated in red) are shown. The number in the bottom panel indicates the percentage of the N-positive area. Summarized data are shown in Figure 4D.

(C) Type II pneumocytes in the lungs of infected hamsters. Right lung lobes of hamsters infected with B.1.1 (n = 4), BA.1 (n = 4), and BA.2 (n = 4) at 5 d.p.i. In each panel, H&E staining (top) and the digitalized inflammation area (bottom, indicated in red) are shown. The number in the bottom panel indicates the percentage of the section represented by the indicated area (i.e., the area indicated in red within the total area of the lung lobe). The panels shown in the left column are identical to those shown in Figure 4H.

Scale bars, 1 mm (A); or 5 mm (B); or 5 mm (C).